SWING-UP AND STABILIZATION OF A CART PENDULUM AND TWIN PENDULUM SYSTEM

Using Nonlinear Control Strategies

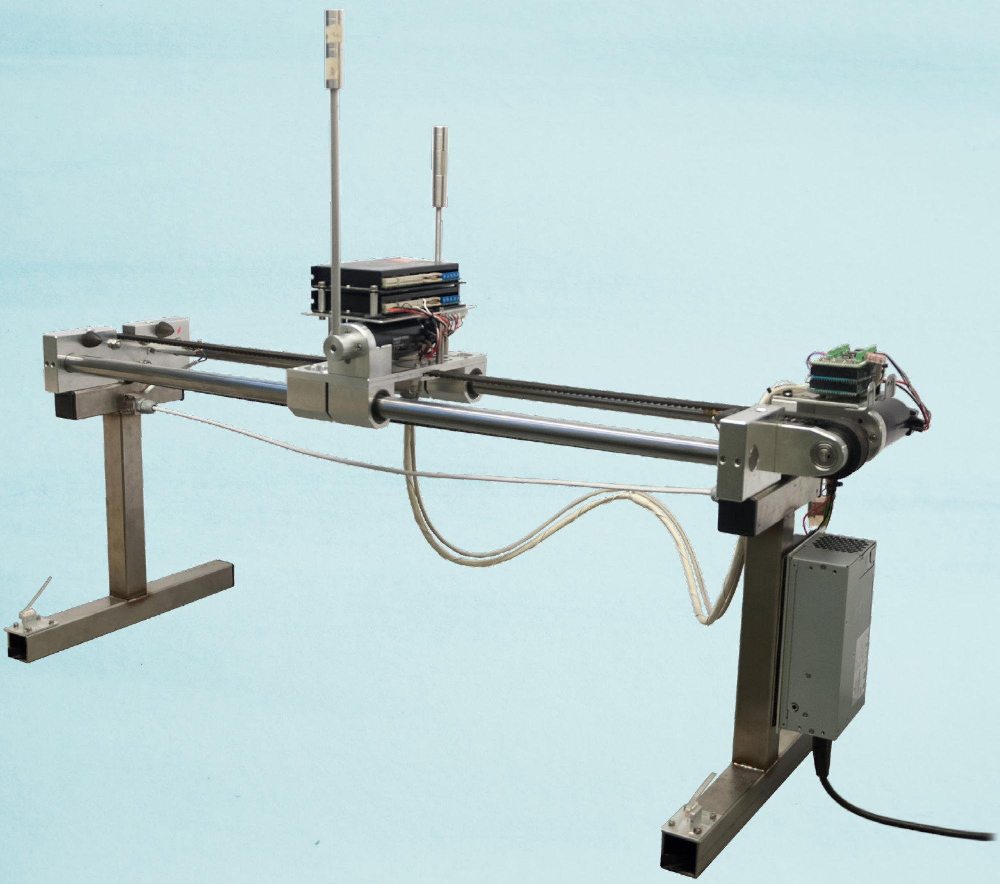

Niels Skov Vestergaard

Master Thesis

Control & Automation

AALBORG UNIVERSITY
DENMARK

AALBORG UNIVERSITY
STUDENT REPORT

Master Thesis

Control and Automation

Department of Electronic Systems

Fredrik Bajers Vej 7C

9220 Aalborg

Title:
Swing-Up and Stabilization of a Cart Pendulum System and Stabilization of a Twin Pendulum System

Subtitle:
Using Nonlinear Control Strategies

Theme:
Nonlinear Control

Project Period:
Autumn 2018

Participants:
Niels Skov Vestergaard

Supervisor:
John-Josef Leth

Pages: ?
Appendices: ?
Attachments: ?

Concluded: 2019-01-16

Synopsis:

Nam dui ligula, fringilla a, euismod sodales, sollicitudin vel, wisi. Morbi auctor lorem non justo. Nam lacus libero, pretium at, lobortis vitae, ultricies et, tellus. Donec aliquet, tortor sed accumsan bibendum, erat ligula aliquet magna, vitae ornare odio metus a mi. Morbi ac orci et nisl hendrerit mollis. Suspendisse ut massa. Cras nec ante. Pellentesque a nulla. Cum sociis natoque penatibus et magnis dis parturient montes, nascetur ridiculus mus. Aliquam tincidunt urna. Nulla ullamcorper vestibulum turpis. Pellentesque cursus luctus mauris.Nam dui ligula, fringilla a, euismod sodales, sollicitudin vel, wisi. Morbi auctor lorem non justo. Nam lacus libero, pretium at, lobortis vitae, ultricies et, tellus. Donec aliquet, tortor sed accumsan bibendum, erat ligula aliquet magna, vitae ornare odio metus a mi. Morbi ac orci et nisl hendrerit mollis. Suspendisse ut massa. Cras nec ante. Pellentesque a nulla. Cum sociis natoque penatibus et magnis dis parturient montes, nascetur ridiculus mus. Aliquam tincidunt urna. Nulla ullamcorper vestibulum turpis. Pellentesque cursus luctus mauris.

Contents

1 | Introduction

This project is concerned with developing nonlinear control strategies for a cart pendulum system and to apply these to the set-up provided in the Control and Automation Lab at Aalborg University (AAU).
The project is two part. The objective of the first part is to design a swing-up controller along with a stabilizing controller to catch the pendulum at the upright position.
In the second part an additional pendulum is attached to the cart in the setup making it a twin pendulum system. The idea is to estimate the additional state and ultimately stabilize the two pendulums in upright position.

Part I

Cart Pendulum

2 | System and Model

A brief overview of the relevant system for *Part 1* is presented in this chapter along with a model of the system.

2.1 System

A setup is provided by the Control and Automation Department at AAU, see Figure 2.1.

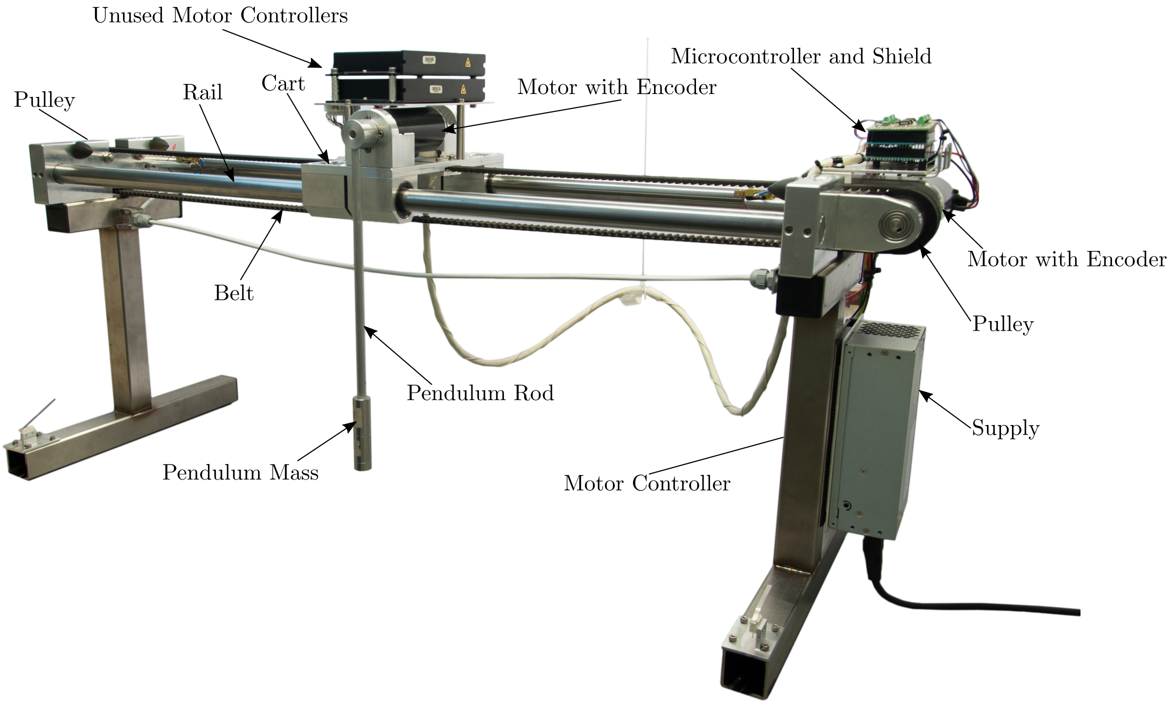

Figure 2.1: The setup provided by AAU. The motor controller in use is not directly visible in this picture as it is mounted behind the power supply.

As seen in Figure 2.1 the belt is attracted by pulleys one of which is driven by a brushed Maxon 370356 DC motor [1]. An other of these maxon motors is mounted on the pendulum but is disconnected and just used as a joint in this project. Both motors are fitted with an HEDS 5540 optical quadrature encoder allowing for relative position and angle of the cart and pendulum respectively [2].

The motor driving the belt is controlled using a Maxon ADS 50/10 motor controller configured in current control mode. The motor controller takes a $\pm 10\,\mathrm{V}$ input signal which then determines the armature current, i_a, see [3].

The primary control unit is a Teensy 3.6 microcontroller board. To program the board through the onboard USB connection a bootloader is used along with the Teensyduino add-on for the Arduino IDE [4].

The encoders are decoded on a shield using Avago HCTL-2021-PLC decoders and read through an 8 bit parallel data bus on the microcontroller board resulting in 2000 tics pr. revolution. This ensures a resolution for the pendulum angle, θ, of $2\pi/2000 = \pi \times 10^{-3}\,\mathrm{rad/tic}$ and $2\pi r/2000 = 2\pi \cdot 0.028/2000 \approx 0.088 \times 10^{-3}\,\mathrm{m/tic}$ for the cart position, x, see [5].

The supply circuit on the microcontroller board is powered by 5V which is regulated to 3.3 V resulting in a $0-3.3\,\mathrm{V}$ range for the 12 bit analog output [6]. This output is used to provide the motor controller with an armature current reference, thus, the microcontroller analog output is amplified through the shield to meet the $\pm 10\,\mathrm{V}$ input requirement of the motor controller [7].

The following relation between analog 12 bit output values, $\mathrm{bit_{DAC}}$, from the microcontroller and armature current in the motor was found by a previous project group [7],

$$\mathrm{bit_{DAC}} = 105.78 \cdot i_a + 1970 \quad , \tag{2.1}$$

and as a result of a force test, see [8], Equation 2.1 was corrected to,

$$\mathrm{bit_{DAC}} = 111.9 \cdot i_a + 1970 \quad , \tag{2.2}$$

which is the relation used in this project. All the system parameters used in the design are listed in Table 2.1. It is assumed that all frictions in the system can be modeled as a combination of Coulomb and viscous frictions. Wires hanging from the cart are unmodeled and their weight along with that of the belt are contained in the estimation of the cart mass.

Parameter	**Notation**	**Quantity**	**Unit**
Nominal current (max. continuous current)	I_{N}	4.58	A
Torque constant	τ_m	93.4×10^{-3}	$\mathrm{N \cdot m \cdot A^{-1}}$
Pendulum Rod Length	l	0.3169	m
Rail Length	l_r	0.89	m
Pulley Radius	r	0.028	m
Pendulum Mass	m	0.2235	kg
Cart Mass	M	6.28	kg
Cart Coulomb Friction	$b_{c,c}$	$f(x, \dot{x})$	N
Cart Viscous Friction	$b_{c,v}$	0	$\mathrm{N \cdot m^{-1}\ s}$
Pendulum Coulomb Friction	$b_{p,c}$	4.1×10^{-3}	$\mathrm{N \cdot m}$
Pendulum Viscous Friction	$b_{p,v}$	0.5×10^{-3}	$\mathrm{N \cdot m \cdot s}$

Table 2.1: The motor parameters, I_{N} and τ_m, are given by maxon in [1]. The rod length is measured from the pendulum pivot point to the geometrical center of the pendulum mass. Pulley radius, rail length, pendulum mass and rod length, are measured parameters, while cart mass is estimated same as all frictions. The cart Coulomb friction turns out to be a function of the cart position in addition to velocity. Details on parameter estimation are found in the implementation section at the end of *Part 1*.

2.2 Model

The model is based on the generalized coordinates presented in Figure 2.2.

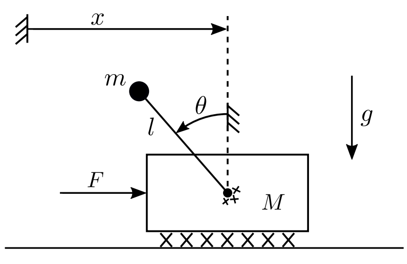

Figure 2.2: Mechanical drawing of the system, where θ is the angle of the pendulum, x is the position of the center of the cart along the rail, F is the applied force and g is the gravitational acceleration. It is indicated that friction is modeled between cart and rail as well as in the pendulum joint.

The pendulum mass center is positioned at zero hight at rest s.t. all energies in the system are positive. It is assumed that the pendulum rod is rigid and massless and that the pendulum weights are a point mass at the geometrical center of the weights.
The motor torque is given by direct relation to the armature current by the motor con-

stant, $\tau_m = k_\tau i_a$, such that,

$$F = \tfrac{1}{r} k_\tau i_a \quad . \tag{2.3}$$

To avoid excessive notation $u = F$ is considered to be the control input in the remaining of this thesis, while keeping in mind the relation in Equation 2.3 along with the knowledge that u must be converted to armature current in implementation.

It is well known that the potential energy, U, and the kinetic energy, T, are given by, [9]

$$U = mgl(1 + \cos\theta) \tag{2.4}$$

$$T = \frac{1}{2}(M+m)\dot{x}^2 - m\dot{x}l\cos\theta\dot{\theta} + \frac{1}{2}ml^2\dot{\theta}^2 \quad . \tag{2.5}$$

The frictions, indicated in Figure 2.2, are, as mentioned, comprised of Coulomb and viscous frictions with values stated in Table 2.1. The viscous frictions are modeled as linear functions of velocities, [10, 11]

$$b_{p,v}\dot{\theta} \quad , \qquad b_{c,v}\dot{x} \quad , \tag{2.6}$$

for the rotational and linear case respectively. The coulomb frictions are modeled as a constant with its sign depending on the signs of the velocities, such that, [10, 11]

$$\mathrm{sgn}(\dot{\theta})b_{p,c} \quad , \qquad \mathrm{sgn}(\dot{x})b_{c,c} \quad . \tag{2.7}$$

This, however, introduces discontinuities at zero velocities. Thus, tanh-functions are used to obtain a continues approximation of the sign-functions,

$$\tanh(\mathrm{k_{tanh}}\dot{\theta})b_{p,c} \quad , \qquad b_{c,v}\dot{x} - \tanh(\mathrm{k_{tanh}}\dot{x})b_{c,c} \quad , \tag{2.8}$$

where $\mathrm{k_{tanh}} = 250$ to increase the steepness of the tanh-functions thereby obtaining a closer approximation of the sign-functions. Finally, by use of the Lagrange-d'Alembert Principle, [9]

$$\frac{d}{dt}\frac{\partial\mathcal{L}}{\partial\dot{\mathbf{q}}} - \frac{\partial\mathcal{L}}{\partial\mathbf{q}} = \mathbf{Q} \quad , \tag{2.9}$$

$$\mathbf{q} = \begin{bmatrix} \theta \\ x \end{bmatrix} \quad , \quad \mathbf{Q} = \begin{bmatrix} -b_{p,v}\dot{\theta} - \tanh(\mathrm{k_{tanh}}\dot{\theta})b_{p,c} \\ \frac{1}{r}k_\tau i_a - b_{c,v}\dot{x} - \tanh(\mathrm{k_{tanh}}\dot{x})b_{c,c} \end{bmatrix} \quad , \tag{2.10}$$

and $\mathcal{L} = \mathcal{T} - \mathcal{U}$, the dynamics of the system are found,

$$ml^2\ddot{\theta} - ml\cos\theta\ddot{x} - mgl\sin\theta = -b_{p,v}\dot{\theta} - \tanh(\mathrm{k_{tanh}}\dot{\theta})b_{p,c} \tag{2.11}$$

$$(M+m)\ddot{x} + ml\sin\theta\dot{\theta}^2 - ml\cos\theta\ddot{\theta} = u - b_{c,v}\dot{x} - \tanh(\mathrm{k_{tanh}}\dot{x})b_{c,c} \quad . \tag{2.12}$$

By setting up the dynamic equations, Equation 2.12 and 2.11, in the following manner,

$$
\begin{aligned}
&\begin{bmatrix} ml^2 & -ml\cos\theta \\ -ml\cos\theta & M+m \end{bmatrix} \begin{bmatrix} \ddot{\theta} \\ \ddot{x} \end{bmatrix} + \begin{bmatrix} 0 \\ ml\sin\theta\dot{\theta}^2 \end{bmatrix} + \\
&+ \begin{bmatrix} b_{p,v}\dot{\theta} + \tanh(\mathrm{k}_{\mathrm{tanh}}\dot{\theta})b_{p,c} \\ b_{c,v}\dot{x} + \tanh(\mathrm{k}_{\mathrm{tanh}}\dot{x})b_{c,c} \end{bmatrix} + \begin{bmatrix} -mgl\sin\theta \\ 0 \end{bmatrix} = \begin{bmatrix} 0 \\ u \end{bmatrix} \quad ,
\end{aligned}
\tag{2.13}
$$

the general form of an m-link robot is obtained, [12, 13]

$$
\mathbf{M}(\mathbf{q})\ddot{\mathbf{q}} + \mathbf{C}(\mathbf{q},\dot{\mathbf{q}}) + \mathbf{B}(\dot{\mathbf{q}}) + \mathbf{G}(\mathbf{q}) = \mathbf{F} \quad , \tag{2.14}
$$

where,

$\mathbf{M}(\mathbf{q})$	is the inertia matrix
$\mathbf{C}(\mathbf{q},\dot{\mathbf{q}})$	is the Coriolis and centrifugal effects
$\mathbf{B}(\dot{\mathbf{q}})$	is the friction
$\mathbf{G}(\mathbf{q})$	is the force due to gravity
$\mathbf{F}$	is the input force vector .

Choosing $[\; x_1 \;\; x_2 \;\; x_3 \;\; x_4 \;]^{\mathrm{T}} = [\; \theta \;\; x \;\; \dot{\theta} \;\; \dot{x} \;]^{\mathrm{T}}$ as states results in the following nonlinear state space representation,

$$
\begin{bmatrix} \dot{x_1} \\ \dot{x_2} \\ \dot{x_3} \\ \dot{x_4} \end{bmatrix} = \begin{bmatrix} x_3 \\ x_4 \\ \mathbf{M}^{-1}(x_1)(\mathbf{F} - \mathbf{C}(x_1,x_3) - \mathbf{B}(x_3,x_4) - \mathbf{G}(x_1)) \end{bmatrix} \quad , \tag{2.15}
$$

which is convenient when simulating the system. This representation is also used in the control designs.

3 | Swing-Up Design

In this chapter three swing-up controllers are designed, all based on [14]. The pendulum is started at rest, $\theta = \pi$, with the angle convention specified in Figure 2.2. The idea of the swing-up controller is to increase the mechanical energy in the system until it matches that of the desired end state, $\theta = 0$ and $\dot{\theta} = 0$, that is, the upright position at rest. The minimum energy in the system occurs at the starting position at rest, which is considered to be zero as mentioned in the *Model* section 2.2. So the target energy is $E_{\text{eq}} = 2mgl$, that is, the potential energy of the pendulum in the unstable equilibrium.

Consider the pendulum dynamics from Equation 2.12, where $J = ml^2$ is the pendulum inertia and frictions are assumed to be zero such that,

$$J\ddot{\theta} - ml\cos\theta a_c - mgl\sin\theta = 0 \quad . \tag{3.1}$$

This equation captures the behavior of the pendulum corresponding to some controlled acceleration a_c at the pivot point. This acceleration is viewed as the control input for now. The force needed to achieve this acceleration is considered at the end of the design. It is further convenient to describe the energy of the pendulum with the coordinate frame fixed at its pivot point, see Figure 3.1.

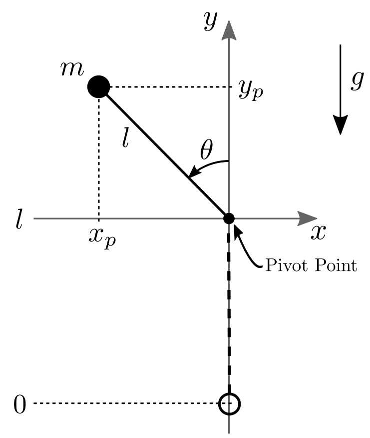

Figure 3.1: The energy used in the swing-up controller is described using this convention, where the coordinate frame is fixed at the pivot point of the pendulum. The zero reference is placed as before s.t. all energies are positive.

From Figure 3.1, the conversion from excessive to generalized coordinates is given by,

$$x_p = -l\sin\theta \quad , \quad y_p = l(\cos\theta + 1) \quad , \quad \dot{x}_p = -l\cos\theta\dot{\theta} \quad , \quad \dot{y}_p = -l\sin\theta\dot{\theta} \quad . \tag{3.2}$$

The mechanical energy in this coordinate frame is then,

$$E_p = mgy_p + \tfrac{1}{2}m\dot{x}_p^2 + \tfrac{1}{2}m\dot{y}_p^2 \tag{3.3}$$
$$E_p = mgl(\cos\theta + 1) + \tfrac{1}{2}m(-l\cos\theta\dot{\theta})^2 + \tfrac{1}{2}m(-l\sin\theta\dot{\theta})^2 \tag{3.4}$$
$$E_p = mgl(\cos\theta + 1) + \tfrac{1}{2}J(\cos^2\theta + \sin^2\theta)\dot{\theta}^2 \tag{3.5}$$
$$E_p = \tfrac{1}{2}J\dot{\theta}^2 + mgl(\cos\theta + 1) \quad . \tag{3.6}$$

The following sections explores different approaches of controlling the pendulum energy specified in Equation 3.6 to its desired reference.

3.1 Energy Control

A function candidate is proposed,

$$V(\theta, \dot{\theta}) = \tfrac{1}{2}E_\Delta^2 \quad , \tag{3.7}$$

where E_Δ is the difference in energy in relation to the unstable equilibrium,

$$E_\Delta = E_p - E_{\mathrm{eq}} \tag{3.8}$$
$$E_\Delta = \tfrac{1}{2}J\dot{\theta}^2 + mgl(\cos\theta + 1) - 2mgl \tag{3.9}$$
$$E_\Delta = \tfrac{1}{2}J\dot{\theta}^2 + mgl(\cos\theta - 1) \quad , \tag{3.10}$$

hence,

$$V = \tfrac{1}{2}(\tfrac{1}{2}J\dot{\theta}^2 + mgl(\cos\theta - 1))^2 \tag{3.11}$$
$$V = \tfrac{1}{2}(\tfrac{1}{2}J\dot{\theta}^2)^2 + \tfrac{1}{2}(mgl(\cos\theta - 1))^2 + \tfrac{1}{2}J\dot{\theta}^2 mgl(\cos\theta - 1) \tag{3.12}$$
$$V = \tfrac{1}{8}J^2\dot{\theta}^4 + \tfrac{1}{2}m^2g^2l^2(\cos^2\theta + 1 - 2\cos\theta) + \tfrac{1}{2}J\dot{\theta}^2 mgl(\cos\theta - 1) \quad , \tag{3.13}$$

further,

$$\frac{\partial V}{\partial \theta} = -m^2g^2l^2\cos\theta\sin\theta + m^2g^2l^2\sin\theta - \tfrac{1}{2}J\dot{\theta}^2 mgl\sin\theta \tag{3.14}$$
$$\frac{\partial V}{\partial \dot{\theta}} = \tfrac{1}{2}J^2\dot{\theta}^3 + Jmgl(\cos\theta - 1)\dot{\theta} \quad , \tag{3.15}$$

where both Equation 3.14 and 3.15 are continuous, C^0, so $V(\theta, \dot{\theta})$ is continuously differentiable, C^1, in the entire $\mathbb{R}^2$.

The idea is to reach the reference $E_\Delta = 0$, which happens when,

$$\tfrac{1}{2}J\dot{\theta}^2 + mgl(\cos\theta - 1) = 0 \tag{3.16}$$
$$\dot{\theta} = \pm\left(\frac{-2mgl(\cos\theta - 1)}{J}\right)^{\frac{1}{2}} \quad . \tag{3.17}$$

A plot of Equation 3.17 in the phase plane, see Figure 3.2, reveals a set of solutions joining the two unstable equilibrium points.

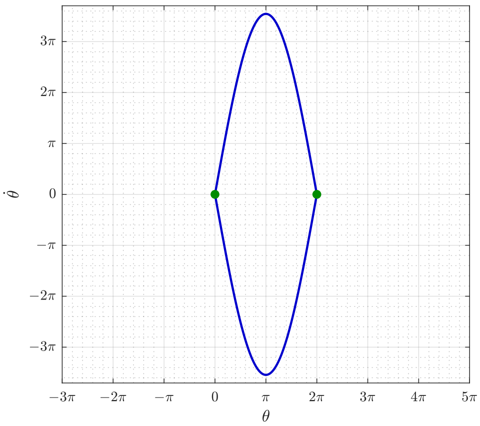

Figure 3.2: If the trajectories of the system are restricted to this set, the energy error is maintained at zero and the trajectories form a heteroclinic orbit.

If the energy reference is successfully tracked, the system will be restricted to this set rather than a single equilibrium point. Such a trajectory joining two equilibrium points is called a heteroclinic orbit.
Recall the system from Equation 3.1,

$$J\ddot{\theta} = ml\cos\theta a_c + mgl\sin\theta \quad , \tag{3.18}$$

the derivative of V is then evaluated along trajectories of the system,

$$\dot{V} = E_\Delta \dot{E}_\Delta \tag{3.19}$$
$$\dot{V} = E_\Delta(J\dot{\theta}\ddot{\theta} - mgl\sin\theta\dot{\theta}) \tag{3.20}$$
$$\dot{V} = E_\Delta(\dot{\theta}(ml\cos\theta a_c + mgl\sin\theta) - mgl\sin\theta\dot{\theta}) \tag{3.21}$$
$$\dot{V} = mlE_\Delta\cos\theta\dot{\theta}a_c \quad . \tag{3.22}$$

The idea is to find a control law, a_c, which allows trajectories of the system to reach the desired heteroclinic orbit. By studying LaSalle's Theorem 3.1.1, analysis of convergence to sets is made possible.

Theorem 3.1.1 (LaSalle's Theorem) *Consider the autonomous system,* $f(\mathbf{x}) = \dot{\mathbf{x}}$, *where* $f : \mathbb{D} \to \mathbb{R}^n$ *is locally Lipschitz and* $\mathbf{x} = \mathbf{0}$ *is an equilibrium point. Then if there exist some function* $V : \mathbb{D} \to \mathbb{R}$ *and*

1. $V(\mathbf{x})$ *is* C^1
2. $\exists\, c > 0$ *s.t.* $\Omega_c = \{\mathbf{x} \in \mathbb{R}^n \mid V(\mathbf{x}) \le c\} \subset \mathbb{D}$ *is bounded*
3. $\dot{V}(\mathbf{x}) \le 0 \quad \forall\, \mathbf{x} \in \Omega_c$

then $\mathbf{x}(0) \in \Omega_c \Rightarrow \mathbf{x}(t) \xrightarrow{t\to\infty} M$, *where* M *is the largest invariant set in*

$E = \{\mathbf{x} \in \Omega_c \mid \dot{V}(\mathbf{x}) = 0\}$ *[15].*

The first condition in LaSalle's Theorem 3.1.1 is already satisfied. Notice that the function candidate, $V(\mathbf{x})$, is not required to be positive definite.
The second condition states that some bounded set, Ω_c, of solutions for which $V(\mathbf{x})$ is less than or equal to some constant c must exist.
This ties into the third condition stating that the derivative of the function candidate must be negative semi-definite along trajectories of the system for all solutions in said set.
The controlled acceleration at the pivot point, a_c, is then designed to satisfy the third condition in Theorem 3.1.1,

$$a_c = -kE_\Delta \cos\theta\dot{\theta} \quad , \tag{3.23}$$

where the tuning parameter, $k > 0$, is introduced to allow scaling the control output to fit the capabilities of the actuator. Inserting the control law yields,

$$\dot{V} = mlE_\Delta \cos\theta\dot{\theta}(-kE_\Delta \cos\theta\dot{\theta}) \tag{3.24}$$

$$\dot{V} = -kml(E_\Delta \cos\theta\dot{\theta})^2 \leq 0 \quad , \tag{3.25}$$

satisfying the third condition of Theorem 3.1.1 not only in Ω_c but in the entire state space. This means any $\infty > c > 0$ will satisfy the second condition. However, looking at the function candidate,

$$V = \tfrac{1}{8}J^2\dot{\theta}^4 + \tfrac{1}{2}m^2g^2l^2(\cos^2\theta + 1 - 2\cos\theta) + \tfrac{1}{2}J\dot{\theta}^2 mgl(\cos\theta - 1) \quad , \tag{3.26}$$

the angle is only present in periodic functions. Hence no value of c can bound the angle. If starting some arbitrary place in the state space, the energy reference is eventually tracked, but the heteroclinic orbit could settle between any two saddle points. To constrain further analysis and design to the desired region of operation, Ω_c is defined as the set containing all points within and on the set in Figure 3.2, that is,

$$\Omega_c = \{\mathbf{x} \mid \dot{\theta} \leq \left(\frac{-2mgl(\cos\theta - 1)}{J}\right)^{\frac{1}{2}}, \ 0 \leq \theta \leq 2\pi\} \quad . \tag{3.27}$$

All conditions of LaSalle's Theorem 3.1.1 are satisfied, thus, if starting in Ω_c, trajectories of the system will converge to M as time goes to infinity. M is the largest invariant set in E, which can be described as the union of sets for which Equation 3.25 is zero,

$$A = \{\mathbf{x} \in \Omega_c \mid E_\Delta = 0\} \tag{3.28}$$

$$B = \{\mathbf{x} \in \Omega_c \mid \ \cos\theta = 0\} \tag{3.29}$$

$$C = \{\mathbf{x} \in \Omega_c \mid \dot{\theta} = 0\} \tag{3.30}$$

$$E = A \cup B \cup C \quad . \tag{3.31}$$

To construct set M it is necessary to evaluate each set for invariance with respect to the controlled system. A proof is developed to show invariance of set A. Recall the relation between $\dot{\theta}$ and θ for $E_\Delta = 0$,

$$\dot{\theta}_z = \pm\left(\frac{-2mgl(\cos\theta - 1)}{J}\right)^{\frac{1}{2}} \quad , \tag{3.32}$$

where $\dot{\theta}_z$ is the angular velocity for which the energy error is zero. Further, consider the controlled system in following form,

$$\ddot{\theta} = \tfrac{1}{J}(-kml\cos\theta E_\Delta \cos\theta\dot{\theta} + mgl\sin\theta) \quad . \tag{3.33}$$

To prove that A is invariant with respect to Equation 3.33, the slope of $\dot{\theta}_z$ is compared to the slope of the controlled system trajectories in the set. If the slopes are equal, then no trajectory can leave the set A, thus proving A is invariant with respect to the controlled system. The slope of $\dot{\theta}_z$ is,

$$\frac{\partial\dot{\theta}_z}{\partial\theta} = \pm\frac{mgl\sin\theta}{J}\left(\frac{-2mgl(\cos\theta - 1)}{J}\right)^{-\frac{1}{2}} \tag{3.34}$$

$$\frac{\partial\dot{\theta}_z}{\partial\theta} = \frac{mgl\sin\theta}{J\dot{\theta}_z} \quad . \tag{3.35}$$

The slope of the trajectories of the controlled system, Equation 3.33, in set A is then,

$$b = \frac{\ddot{\theta}_z}{\dot{\theta}_z} \tag{3.36}$$

$$b = \frac{-kml\cos^2\theta E_\Delta(\theta,\dot{\theta}_z)\dot{\theta}_z + mgl\sin\theta}{J\dot{\theta}_z} \tag{3.37}$$

$$b = \frac{-kml\cos^2\theta(\frac{1}{2}J\dot{\theta}_z^2 + mgl(\cos\theta - 1))\dot{\theta}_z}{J\dot{\theta}_z} + \frac{mgl\sin\theta}{J\dot{\theta}_z} \tag{3.38}$$

$$b = -kml\cos^2\theta\tfrac{1}{2}\dot{\theta}_z^2 - \tfrac{1}{J}kml\cos^2\theta mgl(\cos\theta - 1) + \frac{mgl\sin\theta}{J\dot{\theta}_z} \tag{3.39}$$

$$b = -kml\cos^2\theta\tfrac{1}{2}\left(\frac{-2mgl(\cos\theta - 1)}{J}\right) - \tfrac{1}{l^2m}km^2l^2g\cos^2\theta(\cos\theta - 1) + \frac{mgl\sin\theta}{J\dot{\theta}_z} \tag{3.40}$$

$$b = -kml\cos^2\theta\tfrac{1}{2}\frac{-2mgl(\cos\theta - 1)}{l^2m} - k\cos^2\theta mg(\cos\theta - 1) + \frac{mgl\sin\theta}{J\dot{\theta}_z} \tag{3.41}$$

$$b = k\cos^2\theta mg(\cos\theta - 1) - k\cos^2\theta mg(\cos\theta - 1) + \frac{mgl\sin\theta}{J\dot{\theta}_z} \tag{3.42}$$

$$b = \frac{mgl\sin\theta}{J\dot{\theta}_z} \quad , \tag{3.43}$$

where $\ddot{\theta}_z$ is the angular acceleration of the controlled system in set A.
Finally, since,

$$\frac{\partial\dot{\theta}_z}{\partial\theta} = b \quad , \tag{3.44}$$

the set A is invariant with respect to the controlled system. The set B is invariant only for the intersection $B \cap A$, any other values of the angular velocity will cause it to leave the set since $\cos\theta = 0$ corresponds to a horizontal position of the pendulum. A similar argument can be made for set C, however, in this case if $\theta = \pi$, the system stays in the set. So, the invariant part of set C excluding A is,

$$F = \{\mathbf{x} \in \Omega_c \mid \dot{\theta} = 0 \ , \ \theta = \pi\} \quad , \tag{3.45}$$

thus the largest invariant set in E is,

$$M = A \cup F \quad . \tag{3.46}$$

The sets are visualized in Figure 3.3.

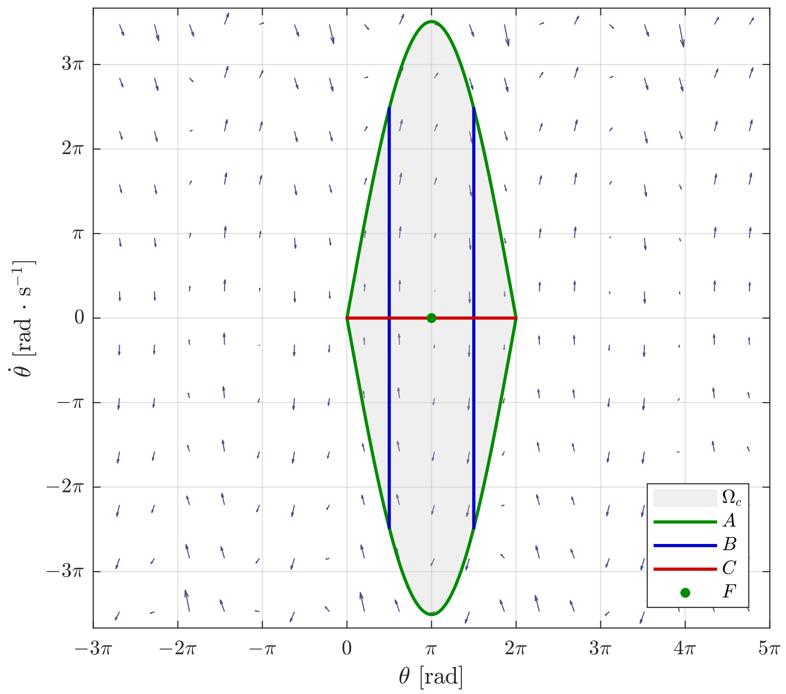

Figure 3.3: The set Ω_c shown along with sets in Ω_c for which $\dot{V}(\mathbf{x}) = 0$. Set A and F together form the largest invariant set M in E. The phase portrait of the controlled system shows how its trajectories line up with A indicating invariance of A with respect to the controlled system.

If this control law is started at zero angular velocity, $\dot{\theta} = 0$, in the stable equilibrium, the computed control is maintained at zero and the pendulum never swings up. So for this control law to work, the pendulum must be started slightly away from the stable equilibrium.

An extra step is needed to apply this control strategy. So far the control output is an acceleration, a_c, at the pivot point. It is possible to input the desired acceleration, a_c, into the second dynamic equation, Equation 2.12, and solve for the force needed to achieve this acceleration,

$$u = (M + m)a_c + ml \sin x_1 x_3^2 - ml \cos x_1 \dot{x}_3 \quad , \tag{3.47}$$

where the cart friction coefficients are set to zero again.
To calculate the force from this expression, Equation 3.47, it is also necessary to know the angular acceleration of the pendulum, $\dot{x}_3$, which can be solved for in the system dynamics, Equation 2.15, inserting known states and control input applied in the previous step,

$$\begin{bmatrix} \dot{x}_3 \\ \dot{x}_4 \end{bmatrix} = \begin{bmatrix} ml^2 & -ml\cos x_1 \\ -ml\cos x_1 & M+m \end{bmatrix}^{-1} \begin{bmatrix} -b_{p,v}x_3 - \tanh(\mathrm{k}_{\tanh}x_3)b_{p,c} + mgl\sin x_1 \\ u_{last} - ml\sin x_1 x_3^2 \end{bmatrix} \quad , \tag{3.48}$$

where u_{last} is the force applied in the previous step.
From Equation 3.48 the approximated angular acceleration is then,

$$\dot{x}_3 = \frac{(M+m)(-b_{p,v}x_3 - \tanh(\mathrm{k}_{\tanh}x_3)b_{p,c} + mgl\sin x_1)}{l^2 m(M+m-m\cos^2 x_1)} + \frac{\cos x_1(u_{last} - ml\sin x_1 x_3^2)}{l(M+m-m\cos^2 x_1)} \quad . \tag{3.49}$$

Inserting Equation 3.49 into Equation 3.47 results in the control input, u, necessary to achieve the desired acceleration, a_c, at the pivot point. This method is used for all three swing-up controllers, so to avoid excessive notation the proceeding energy control laws are derived with a_c as the control parameter.

All simulations are performed using the nonlinear state space representation in Equation 2.15 and the matlab ODE45 solver with a relative tolerance of 1×10^{-7}. Initializing the angle, θ, at $\pi - 0.1$ to avoid zero control output as discussed, the energy difference struggles to reach its reference at zero, see Figure 3.4. The pendulum friction and cart inertia are included in the calculation of the force needed to obtain the desired acceleration. This, however, is not concerned with what is needed to obtain the required energy. So the offset seen in Figure 3.4 is caused by the control law, Equation 3.23, asking for insufficient acceleration.

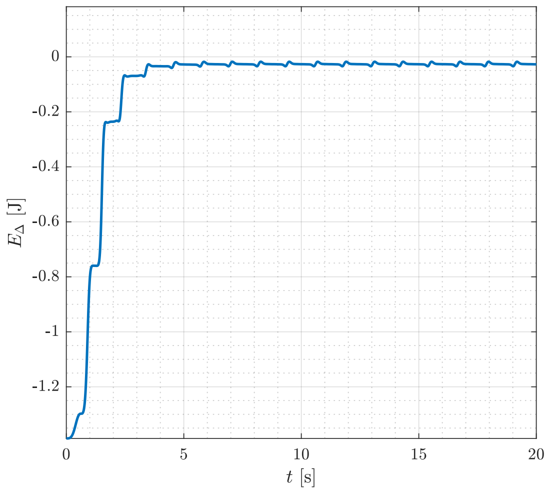

Figure 3.4: Simulation of the first energy control method. The energy error struggles to maintain zero value, due to pendulum friction and cart inertia exchanging energy with the pendulum.

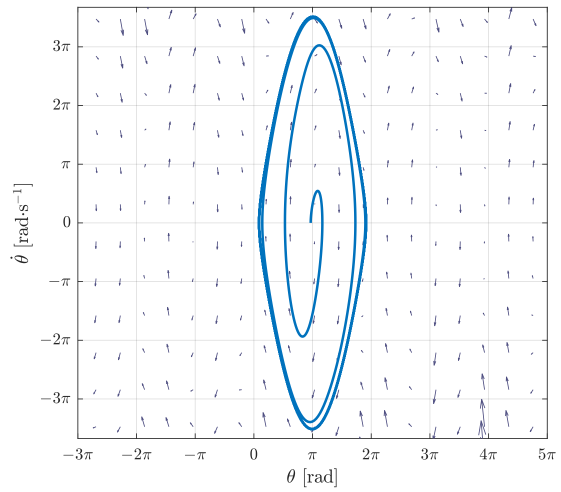

Figure 3.5: This phase portrait shows the attempt to reach the heteroclinic orbit. It falls short due to the insufficient acceleration asked by the control law.

The pendulum also falls short of reaching the heteroclinic orbit, see Figure 3.5. Further, since the energy of the pendulum is not affected by the position or velocity of the cart, this control law, Equation 3.23, is not concerned with controlling these. This becomes a problem in the physical setup as it has a rail length of 0.89 m, see Table 2.1. A traced animation is used to demonstrate this problem in Figure 3.6.

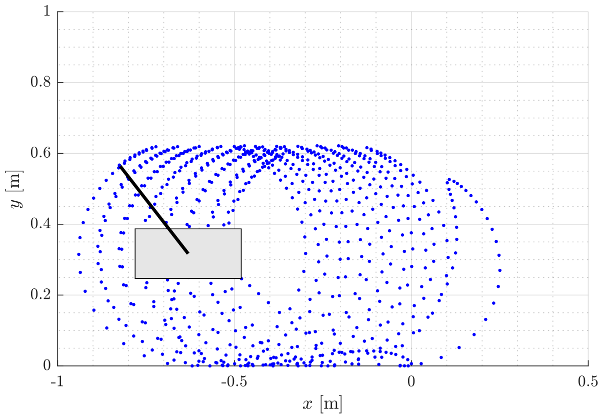

Figure 3.6: The cart drifts beyond the bounds of the physical system. This might not be a problem if the catch controller catches the pendulum in first try, but there is no guarantee of this being the case.

An other issue is the actuation which is limited in the real system by the maximum allowed continuous current, see Table 2.1. By tuning the parameter k in the control law, better performance can be obtained, however at the cost of excessive actuation.

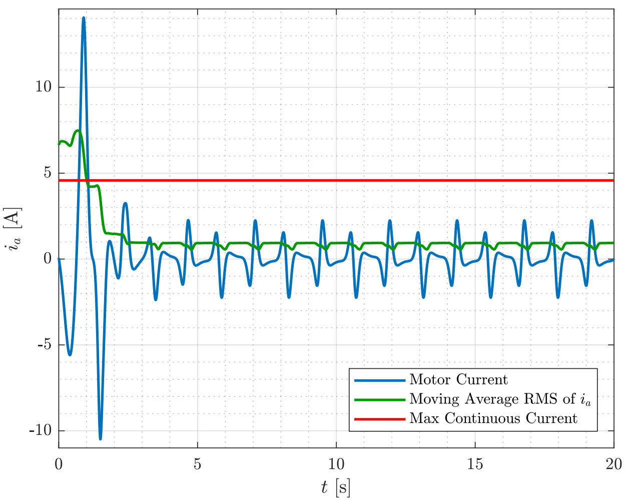

Figure 3.7: The motor current has high peaks in the beginning which likely exceeds the capabilities of the motor. The controller is tuned such that the RMS value of the current does not exceed the maximum continuous current requirement of the motor for a sustained period of time.

For these graphs $k = 1.3$ to keep the motor current at acceptable levels. The motor current is shown in Figure 3.7 where the rolling RMS of i_a is used to approximate the continuous current load on the motor. Though the continuous current is acceptable, the peaks in the start will be saturated in the real system, which would cause a longer rise time for the energy.

3.2 Sign-Based Energy Control

There are other ways to satisfy Equation 3.25 than the control law suggested in Equation 3.23. To achieve maximal actuation a sign-function can be used to determine the direction of actuation along with a gain k to adjust for the limits of the actuator as before,

$$a_c = k\ \mathrm{sgn}(-E_\Delta \cos\theta\dot{\theta}) \quad , \tag{3.50}$$

where,

$$\mathrm{sgn}(s(\theta,\dot{\theta})) = \begin{cases} 1 & s > 0 \ \vee\ \cos\theta\dot{\theta} = 0 \\ 0 & s = 0 \ \wedge\ \cos\theta\dot{\theta} \neq 0 \\ -1 & s < 0 \end{cases} \quad , \tag{3.51}$$

to avoid no actuation when starting at stable equilibrium. This adjustment reduces the set,

$$M = \{\mathbf{x} \in \Omega_c \mid E_\Delta = 0\} \quad , \tag{3.52}$$

such that convergence to M when starting in Ω_c, by Theorem 3.1.1, now assures convergence to the energy reference and thus to the heteroclinic orbit.
The gain is tuned to $k = 2.4$ in the following simulation. Looking at the energy in Figure 3.8, this strategy seems to work really well. From the phase portrait in Figure 3.9 it is evident that a near perfect heteroclinic orbit is reached.

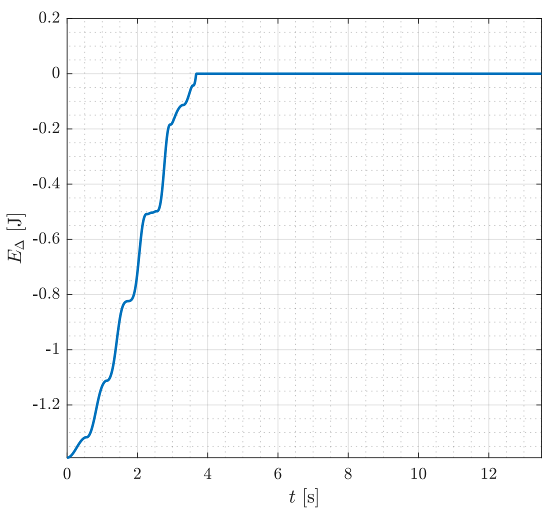

Figure 3.8: Using maximum actuation in the appropriate direction drives the energy error to zero and keeps it there.

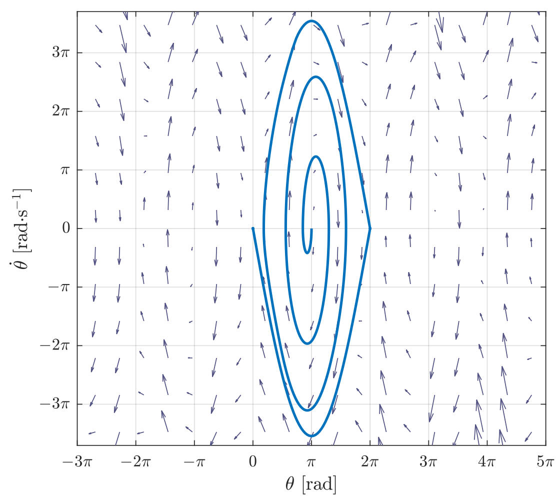

Figure 3.9: The heteroclinic orbit is reached very accurately.

In Figure 3.10 however, while the angle reaches the equilibrium as closely as possible without overshooting, this control law, as with the previous, does not account for position of the cart.

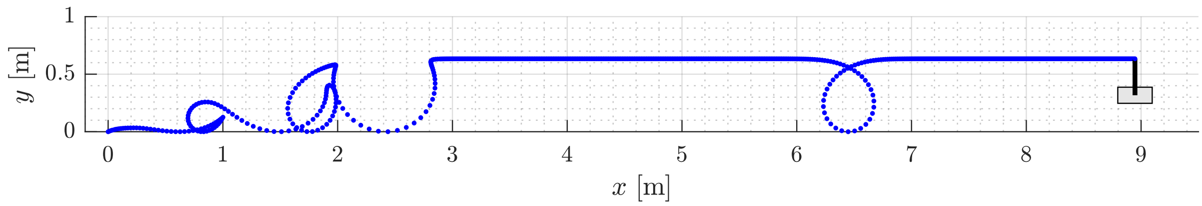

Figure 3.10: The cart drifts as before, since the controller is only concerned with the energy of the pendulum.

However, the bigger problem with this control law is obvious from Figure 3.11, where excessive switching shows on the control output.

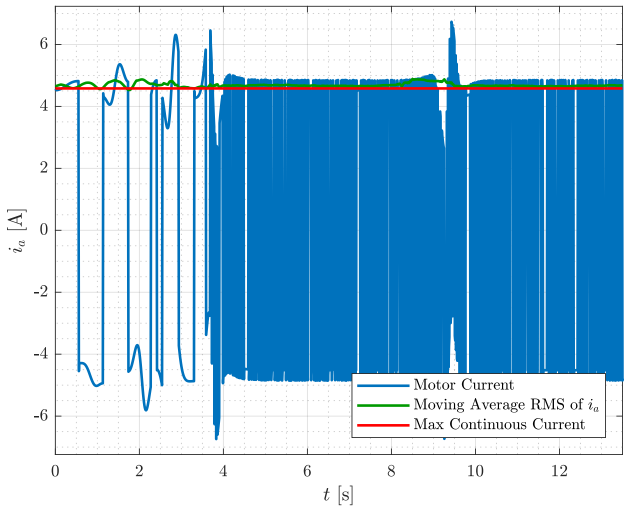

Figure 3.11: The sign-function in the control law causes excessive switching in the output, thus, the design is not feasible for a real system implementation.

This actuation behavior is not feasible in a real system and attempted implementation will cause chattering resulting in unwanted behavior and wear of the motor. In next section it is attempted to solve this issue, while keeping some of the performance of this approach.

3.3 Sat-Based Energy Control

To avoid the excessive switching of the sign-based controller a different strategy using a saturation function is investigated,

$$a_c = \mathrm{sat}(-kE_\Delta \mathrm{sgn}(\cos\theta\dot{\theta})) \quad , \tag{3.53}$$

where

$$\operatorname{sgn}(s) = \begin{cases} 1 & |s| \geq 0 \\ -1 & |s| < 0 \end{cases} , \tag{3.54}$$

and the sat-function saturates at the minimum/maximum allowed acceleration. The known limitation is $i_{max} = 4.58\,\mathrm{A}$ as stated in Table 2.1, from which the maximum control, u, can be calculated,

$$u_{max} = \frac{k_\tau}{r} , \tag{3.55}$$

and finally, by disregarding the pendulum behavior and cart friction from the dynamics in Equation 2.12,

$$a_{max} = \frac{u_{max}}{M+m} . \tag{3.56}$$

As this is a crude estimate $0.1\,\mathrm{m} \cdot \mathrm{s}^{-2}$ is subtracted from the estimated a_{max} in following simulations to stay within the actuation limits. The saturation function is then,

$$\operatorname{sat}(s) = \begin{cases} s & |s| \leq a_{max} \\ \operatorname{sgn}(s)\, a_{max} & |s| > a_{max} \end{cases} . \tag{3.57}$$

Notice how the sgn-function in this control law, Equation 3.53, only takes $\cos\theta\dot{\theta}$ as input. Contrary to the sign-based controller which also included E_Δ causing the need for complicated restrictions in the definition of the sgn-function.

Choice of k decides how aggressive the controller should be. Larger values of k drives the control into saturation faster thus actuating more like the sign-based controller in Equation 3.50. At lower values of k the operation will not reach saturation as fast thus behaving more like the first energy based controller in Equation 3.23. For an effective swing up behavior $k = 200$ is chosen, thus approaching the behavior of the sign-based controller, which makes sense as this is the theoretically ideal solution.
This control strategy achieves the energy reference in about three seconds, Figure 3.12, as is the case of the sign-based strategy, Figure 3.8. Further, from Figure 3.13, the system still reaches a near perfect heteroclinic orbit.

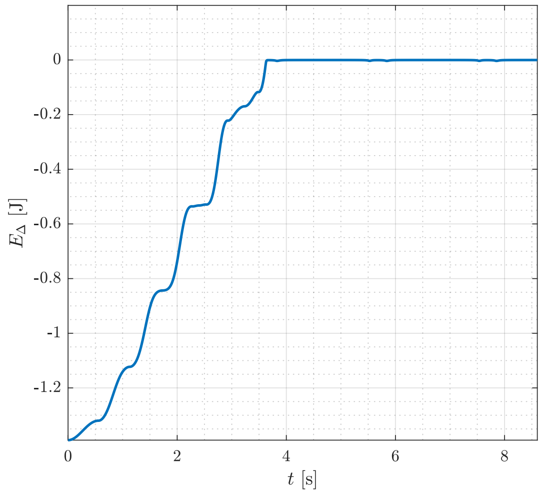

Figure 3.12: The sat-based controller shows no loss in performance when comparing the energy error to that of the sign-based approach.

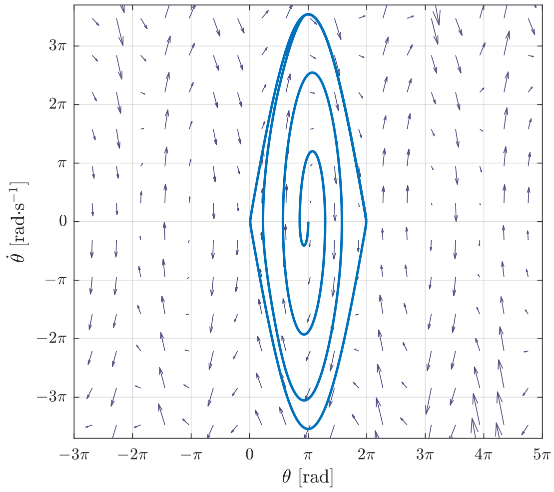

Figure 3.13: The heteroclinic orbit is still reached, however, with a more realistic trajectory at the approach of the equilibrium points.

The cart still drifts as expected, see Figure 3.14, and the equilibrium points are maintained for shorter duration, which is expected with less control switching. Figure 3.14.

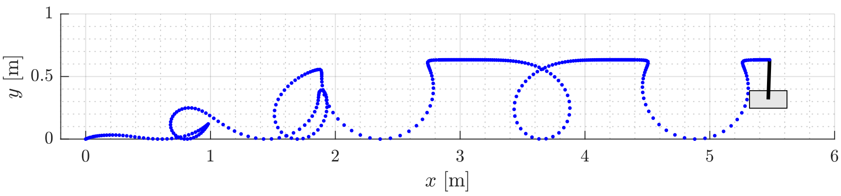

Figure 3.14: This strategy performs well. The drifting problem is solved later.

The excessive switching on the control output is successfully avoided, see Figure 3.15, resulting in a much more realistic control signal compared to that in Figure 3.11.

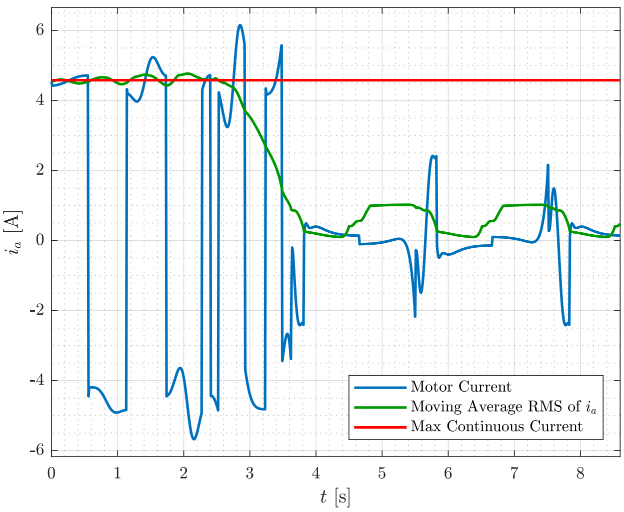

Figure 3.15: The control signal using the sat-based approach is much more realistic for implementation as the excessive switching of the sign-based controller is successfully avoided.

The design of the energy based control law, Equation 3.53, is concluded. The problem of controlling the cart position still remains. In the following, the performance of this control law is subjected to the disturbance caused by added control on the cart position and velocity.

3.4 Cart Position and Velocity Control

To solve the cart drifting problem along x a linear controller is designed and added to the control law,

$$a_c = \psi(x_1, x_3) + v(x_2, x_4) \quad , \tag{3.58}$$

where $\psi(x_1, x_3)$ is the energy controller and $v(x_2, x_4)$ is the linear controller. While these two controllers depend on different states, they still influence and act as unmodeled disturbances to one another. The position and velocity control, $v(x_2, x_4)$, adds and subtracts energy, therefore could cause the energy controller, $\psi(x_1, x_3)$, to overshoot. One solution to this potential problem could be to slightly lower the energy reference. However, swing-up is often designed with a higher energy reference such that the catch controller has some entry velocity at the unstable equilibrium.
With these considerations in mind, the design of $v(x_2, x_4)$ is proceeded. Considering the cart without friction and assuming any influence of the pendulum dynamics and the energy control to be unmodeled disturbances of the system. This reduces the model to the mechanical drawing seen in Figure 3.16.

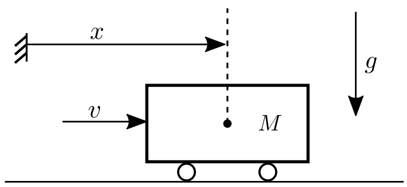

Figure 3.16: Mechanical drawing of the reduced model used for position control.

The dynamics are then,

$$M\ddot{x} = v \quad , \tag{3.59}$$

and selecting new states $[\ z_1 \ \ z_2\ ]^{\mathrm{T}} = [\ x \ \ \dot{x}\ ]^{\mathrm{T}}$, the linear state space is,

$$\begin{bmatrix} \dot{z}_1 \\ \dot{z}_2 \end{bmatrix} = \underbrace{\begin{bmatrix} 0 & 1 \\ 0 & 0 \end{bmatrix}}_{A} \begin{bmatrix} z_1 \\ z_2 \end{bmatrix} + \underbrace{\begin{bmatrix} 0 \\ \frac{1}{M} \end{bmatrix}}_{B} v \quad . \tag{3.60}$$

The closed loop poles are placed in $p = [\ -1 \ \ -2\ ]$ using matlab *place()*-command to obtain linear feedback gains, $\mathbf{k_1} = [\ 10.5460 \ \ 15.8190\ ]$, resulting in the controller,

$$v = -\mathbf{k_1 z} \quad , \tag{3.61}$$

where $\mathbf{z} = [\ x \ \ \dot{x}\ ]^{\mathrm{T}}$, such that,

$$v(x_2, x_4) = -\mathbf{k_1}[\ x_2 \ \ x_4\ ]^{\mathrm{T}} \quad , \tag{3.62}$$

in therms of the full system. This control is added to the sat-based design and simulations are run without changing any previously designed gains.

Figure 3.17 shows the energy error reaching zero, taking one second longer under the influence of the linear controller, compared to Figure 3.12.

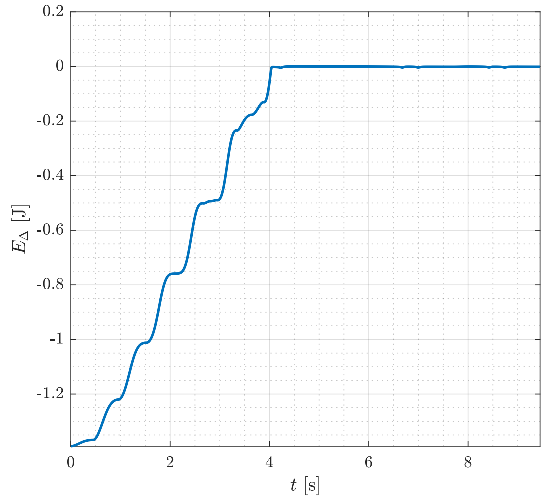

Figure 3.17: The sat-based controller reaches the reference in about four seconds, compared to three seconds it took without position and velocity control.

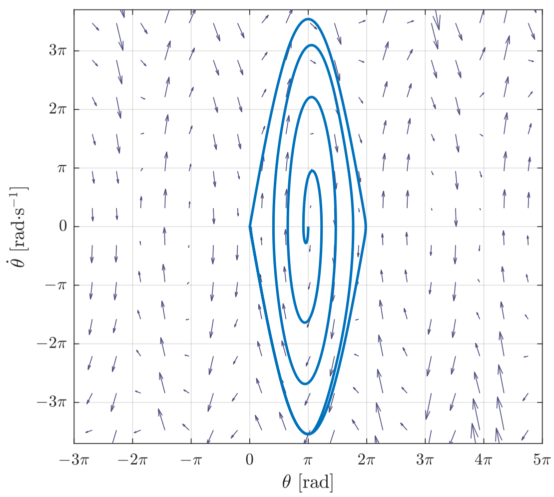

Figure 3.18: Though the sat-based energy controller reaches its reference one second slower when kept around $x = 0$, it still reaches the heteroclinic orbit with no overshoot.

In the phase portrait, see Figure 3.18, it is clear that the sat-based controller still reaches the heteroclinic orbit. Figure 3.19 shows how the linear control of the cart position and velocity successfully keeps the system within the available operating region of the real system.

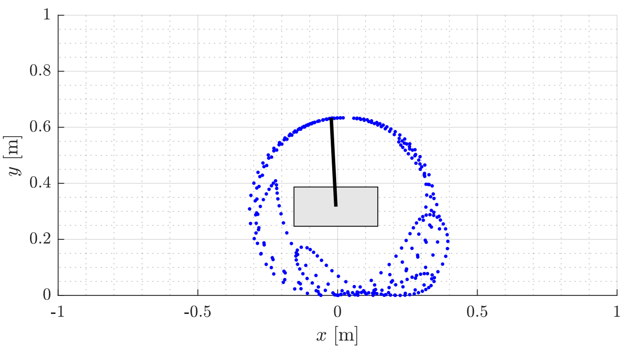

Figure 3.19: The linear control successfully keeps the cart around zero while the energy control approaches the unstable equilibrium.

Figure 3.20 shows the actuation required, the RMS is slightly lower than it was before the linear controller was added.

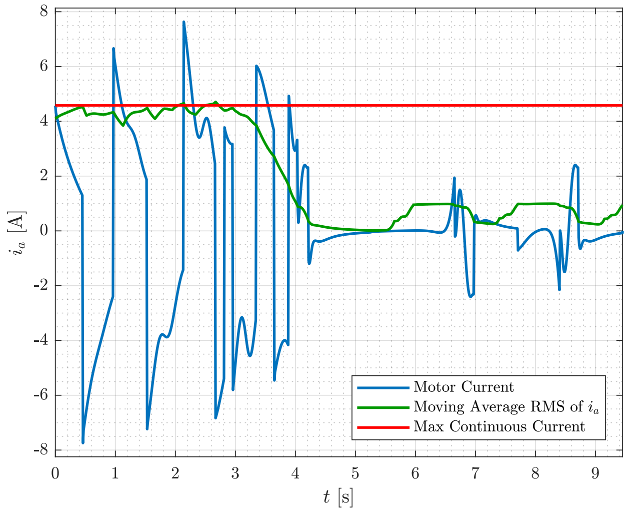

Figure 3.20: The control signal causes less continuous current but higher peaks compared to the same swing-up without control on the cart position.

Figure 3.21 show the position approaching zero as the energy control settles, which is ideal, as it means the energy controller still has room to operate without fighting the linear feedback controller too much. Similarly, the oscillations around zero are necessary for the energy controller to keep its reference. Further, as seen in Figure 3.22 the velocity of the cart is also eventually controlled to zero by the added liner controller.

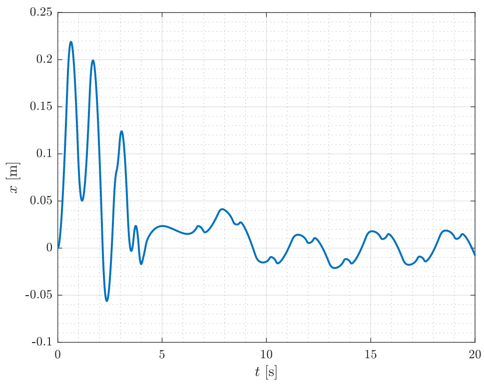

Figure 3.21: The saturation based controller keeps the cart closer to zero, suggesting less actuation from the energy control.

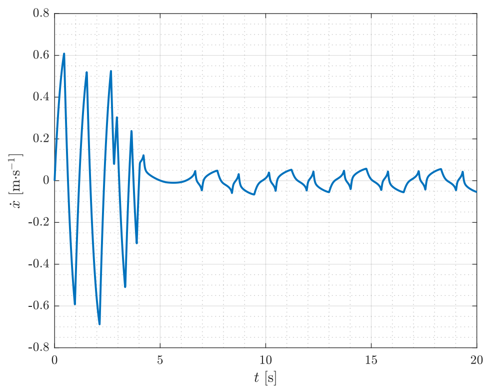

Figure 3.22: Zero velocity is obtained quite effectively after the energy reference is reached.

These two graphs are simulated over longer time to show that the linear controller reaches its reference.

This concludes the design of swing-up control.

4 | Stabilization

In this section the idea is to stabilize the pendulum in the unstable equilibrium. Ultimately this controller should be able to take over from the swing-up controller when some minimum catch angle is reached.
A sliding mode control strategy is employed to accomplish these goals. The design is based on [15].
Firstly, the model of the system, from Equation 2.15, is considered in following form,

$$\begin{bmatrix} \dot{x}_1 \\ \dot{x}_2 \\ \dot{x}_3 \\ \dot{x}_4 \end{bmatrix} = \underbrace{\begin{bmatrix} x_3 \\ x_4 \\ \mathbf{M}^{-1}(x_1)(-\mathbf{C}(x_1,x_3) - \mathbf{B}(x_3,x_4) - \mathbf{G}(x_1)) \end{bmatrix}}_{\mathbf{f}(\mathbf{x})} + \underbrace{\begin{bmatrix} 0 \\ 0 \\ \mathbf{M}^{-1}(x_1)\mathbf{F} \end{bmatrix}}_{\mathbf{g}(\mathbf{x})u} , \tag{4.1}$$

where,

$$\mathbf{M}^{-1} = \begin{bmatrix} \frac{(M+m)}{l^2 m(M+m-m\cos^2 x_1)} & \frac{\cos x_1}{l(M+m-m\cos^2 x_1)} \\ \frac{\cos x_1}{l(M+m-m\cos^2 x_1)} & \frac{1}{M+m-m\cos^2 x_1} \end{bmatrix} , \tag{4.2}$$

with states $[\ x_1 \quad x_2 \quad x_3 \quad x_4\ ]^{\mathrm{T}} = [\ \theta \quad x \quad \dot{\theta} \quad \dot{x}\ ]^{\mathrm{T}}$ and input vector $\mathbf{F} = [\ 0 \quad u\ ]^{\mathrm{T}}$ as before.

In Equation 4.1 the input, u, appear in two of the four state equations. To design a sliding mode controller for the system, it is transformed into *regular form*,

$$\begin{aligned} \dot{\boldsymbol{\eta}} &= \mathbf{f_a}(\boldsymbol{\eta}, \xi) \\ \dot{\xi} &= f_b(\boldsymbol{\eta}, \xi) + g_b(\boldsymbol{\eta}, \xi)u \quad , \end{aligned} \tag{4.3}$$

where the input only appears on one state equation. The transform is then given by,

$$\mathbf{T}(\mathbf{x}) = \begin{bmatrix} \boldsymbol{\eta} \\ \xi \end{bmatrix} \Rightarrow \frac{\partial}{\partial t}\mathbf{T}(\mathbf{x}) = \begin{bmatrix} \dot{\boldsymbol{\eta}} \\ \dot{\xi} \end{bmatrix} \Rightarrow \frac{\partial}{\partial t}\mathbf{T}(\mathbf{x}) = \begin{bmatrix} \mathbf{f_a}(\boldsymbol{\eta}, \xi) \\ f_b(\boldsymbol{\eta}, \xi) + g_b(\boldsymbol{\eta}, \xi)u \end{bmatrix} , \tag{4.4}$$

further,

$$\frac{\partial \mathbf{T}}{\partial t} = \frac{\partial \mathbf{T}}{\partial \mathbf{x}}\dot{\mathbf{x}} \tag{4.5}$$

$$\begin{bmatrix} \mathbf{f_a}(\boldsymbol{\eta}, \xi) \\ f_b(\boldsymbol{\eta}, \xi) + g_b(\boldsymbol{\eta}, \xi)u \end{bmatrix} = \frac{\partial \mathbf{T}}{\partial \mathbf{x}}\mathbf{f}(\mathbf{x}) + \frac{\partial \mathbf{T}}{\partial \mathbf{x}}\mathbf{g}(\mathbf{x})u \quad , \tag{4.6}$$

such that,

$$\frac{\partial \mathbf{T}}{\partial \mathbf{x}}\mathbf{f}(\mathbf{x}) = \begin{bmatrix} \mathbf{f_a}(\boldsymbol{\eta},\xi) \\ f_b(\boldsymbol{\eta},\xi) \end{bmatrix} \quad , \quad \frac{\partial \mathbf{T}}{\partial \mathbf{x}}\mathbf{g}(\mathbf{x}) = \begin{bmatrix} \mathbf{0} \\ g_b(\boldsymbol{\eta},\xi) \end{bmatrix} \quad . \tag{4.7}$$

Equation 4.7 results in the following four equations,

$$\begin{aligned} \frac{\partial \eta_1}{\partial x_3}g_3 + \frac{\partial \eta_1}{\partial x_4}g_4 = 0 \quad &, \quad \frac{\partial \eta_2}{\partial x_3}g_3 + \frac{\partial \eta_2}{\partial x_4}g_4 = 0 \\ \frac{\partial \eta_3}{\partial x_3}g_3 + \frac{\partial \eta_3}{\partial x_4}g_4 = 0 \quad &, \quad \frac{\partial \xi}{\partial x_3}g_3 + \frac{\partial \xi}{\partial x_4}g_4 = g_b(\boldsymbol{\eta},\xi) \quad , \end{aligned} \tag{4.8}$$

where,

$$\begin{bmatrix} g_3 \\ g_4 \end{bmatrix} u = \mathbf{M}^{-1}(x_1)\begin{bmatrix} 0 \\ u \end{bmatrix} \quad \Rightarrow \quad \begin{cases} g_3 = \frac{\cos x_1}{l(M+m-m\cos^2 x1)} \\ g_4 = \frac{1}{M+m-m\cos^2 x_1} \end{cases} . \tag{4.9}$$

The following choice of coordinates to satisfy Equation 4.8 without loss of rank in $\mathbf{T}$, is based on the transform used for input-output linearization in [15].
Choosing output, $h(x) = \theta$ or $h(x) = x$, both results in the relative degree, $\rho = 2$, since the output appears on the second derivatives,

$$\ddot{\theta} = \dot{x}_3 = f_3 + g_3 u \tag{4.10}$$

$$\ddot{x} = \dot{x}_4 = f_4 + g_4 u \quad . \tag{4.11}$$

The suggested transform is then,

$$\mathbf{T}(\mathbf{x}) = \begin{bmatrix} \phi_1(\mathbf{x}) \\ \vdots \\ \phi_{n-\rho}(\mathbf{x}) \\ h(\mathbf{x}) \\ L_f h(\mathbf{x}) \\ \vdots \\ L_f^{\rho-1}h(\mathbf{x}) \end{bmatrix} \quad \Rightarrow \quad \begin{bmatrix} \eta_1 \\ \eta_2 \\ \eta_3 \\ \xi \end{bmatrix} = \begin{bmatrix} \phi_1(\mathbf{x}) \\ \phi_2(\mathbf{x}) \\ h(\mathbf{x}) \\ L_f h(\mathbf{x}) \end{bmatrix} \quad , \tag{4.12}$$

where $L_f h(\mathbf{x})$ is the *Lie derivative* of $h(\mathbf{x})$ along $f(\mathbf{x})$. This results in two possible transforms,

$$h = \theta \quad \Rightarrow \quad \mathbf{T}_1 = \begin{bmatrix} \eta_1 \\ \eta_2 \\ \eta_3 \\ \xi \end{bmatrix} = \begin{bmatrix} \phi_1 \\ \phi_2 \\ x_1 \\ x_3 \end{bmatrix} \quad \text{and} \quad h = x \quad \Rightarrow \quad \mathbf{T}_2 = \begin{bmatrix} \eta_1 \\ \eta_2 \\ \eta_3 \\ \xi \end{bmatrix} = \begin{bmatrix} \phi_1 \\ \phi_2 \\ x_2 \\ x_4 \end{bmatrix} \quad , \tag{4.13}$$

leaving ϕ_1 and ϕ_2 to be determined. This is done by satisfying,

$$\frac{\partial \eta_1}{\partial x_3} g_3 + \frac{\partial \eta_1}{\partial x_4} g_4 = 0 \tag{4.14}$$

$$\frac{\partial \eta_2}{\partial x_3} g_3 + \frac{\partial \eta_2}{\partial x_4} g_4 = 0 \quad , \tag{4.15}$$

from Equation 4.8. For $\mathbf{T}_1$ the choice $\phi_1 = x_2$ satisfies Equation 4.14 with no loss of rank in the transform. Conversely for $\mathbf{T}_2$ the choice $\phi_1 = x_1$ satisfies Equation 4.14 again with no loss of rank. This leaves ϕ_2 which, for both transforms, is determined by finding a solution to Equation 4.15,

$$\frac{\partial \eta_2}{\partial x_3} \frac{\cos x_1}{l(M + m - m\cos^2 x1)} + \frac{\partial \eta_2}{\partial x_4} \frac{1}{M + m - m\cos^2 x_1} = 0 \quad , \tag{4.16}$$

choosing,

$$\frac{\partial \eta_2}{\partial x_4} = \frac{\cos x_1}{l} \quad , \quad \frac{\partial \eta_2}{\partial x_3} = -1 \quad , \tag{4.17}$$

such that,

$$\eta_2 = \frac{\cos x_1}{l} x_4 - x_3 \quad . \tag{4.18}$$

This results in the following two transform candidates,

$$\mathbf{T}_1 = \begin{bmatrix} x_2 \\ \frac{\cos x_1}{l} x_4 - x_3 \\ x_1 \\ x_3 \end{bmatrix} \quad , \quad \mathbf{T}_2 = \begin{bmatrix} x_1 \\ \frac{\cos x_1}{l} x_4 - x_3 \\ x_2 \\ x_4 \end{bmatrix} \quad . \tag{4.19}$$

It is desired for the transform, $\mathbf{T}$, to be continuously differentiable and have a continuously differentiable inverse, $\mathbf{T}^{-1}$. Such a transform is known as a diffeomorphism. Further, $\mathbf{T}$ is a global diffeomorphism iff its Jacobian is nonsingular for all $\mathbf{x} \in \mathbb{R}^n$ and $\lim_{||\mathbf{x}|| \to \infty} ||\mathbf{T}(\mathbf{x})|| = \infty$, [15].
Thus the Jacobian of each transform is computed,

$$\mathbf{J}_1 = \frac{\partial \mathbf{T}_1(\mathbf{x})}{\partial \mathbf{x}} = \begin{bmatrix} 0 & 1 & 0 & 0 \\ -\frac{\sin x_1}{l} x_4 & 0 & -1 & \frac{\cos x_1}{l} \\ 1 & 0 & 0 & 0 \\ 0 & 0 & 1 & 0 \end{bmatrix} \tag{4.20}$$

$$\mathbf{J}_2 = \frac{\partial \mathbf{T}_2(\mathbf{x})}{\partial \mathbf{x}} = \begin{bmatrix} 1 & 0 & 0 & 0 \\ -\frac{\sin x_1}{l} x_4 & 0 & -1 & \frac{\cos x_1}{l} \\ 0 & 1 & 0 & 0 \\ 0 & 0 & 0 & 1 \end{bmatrix} \quad . \tag{4.21}$$

To check for singularity the determinant is found for the two Jacobian matrices,

$$\det(\mathbf{J}_1) = -\frac{\cos x_1}{l} \quad , \quad \det(\mathbf{J}_2) = 1 \quad . \tag{4.22}$$

If $\cos x_1 = 0$ the Jacobian, $\mathbf{J}_1$, becomes singular. This only happens when the pendulum is in a horizontal position, which is outside the operating range of a stabilizing controller. However, the Jacobian, $\mathbf{J}_2$, is nonsingular for all $\mathbf{x} \in \mathbb{R}^4$. Further, $\lim_{||\mathbf{x}|| \to \infty} ||\mathbf{T}_2(\mathbf{x})|| = \infty$ so,

$$\mathbf{T} = \begin{bmatrix} \eta_1 \\ \eta_2 \\ \eta_3 \\ \xi \end{bmatrix} = \begin{bmatrix} x_1 \\ \frac{\cos x_1}{l} x_4 - x_3 \\ x_2 \\ x_4 \end{bmatrix} \quad , \tag{4.23}$$

is a global diffeomorphism and therefore chosen as the final system transform, with the inverse given by,

$$\mathbf{T}^{-1} = \begin{bmatrix} x_1 \\ x_2 \\ x_3 \\ x_4 \end{bmatrix} = \begin{bmatrix} \eta_1 \\ \eta_3 \\ \frac{\cos \eta_1}{l} \xi - \eta_2 \\ \xi \end{bmatrix} \quad . \tag{4.24}$$

The derivative of the transform, Equation 4.23, along the trajectories of the system is,

$$\begin{bmatrix} \dot{\eta}_1 \\ \dot{\eta}_2 \\ \dot{\eta}_3 \\ \dot{\xi} \end{bmatrix} = \begin{bmatrix} \dot{x}_1 \\ \frac{-\sin x_1}{l} \dot{x}_1 x_4 + \frac{\cos x_1}{l} \dot{x}_4 - \dot{x}_3 \\ \dot{x}_2 \\ \dot{x}_4 \end{bmatrix} \tag{4.25}$$

$$\begin{bmatrix} \dot{\eta}_1 \\ \dot{\eta}_2 \\ \dot{\eta}_3 \\ \dot{\xi} \end{bmatrix} = \begin{bmatrix} x_3 \\ \frac{-\sin x_1}{l} x_3 x_4 + \frac{\cos x_1}{l} f_4(\mathbf{x}) + \frac{\cos x_1}{l} g_4(\mathbf{x}) u - f_3(\mathbf{x}) - g_3(\mathbf{x}) u \\ x_4 \\ f_4(\mathbf{x}) + g_4(\mathbf{x}) u \end{bmatrix} \quad , \tag{4.26}$$

from which the *regular form* is obtained by rearranging and using the inverse transform,

$$\begin{bmatrix} \dot{\eta}_1 \\ \dot{\eta}_2 \\ \dot{\eta}_3 \\ \hline \dot{\xi} \end{bmatrix} = \begin{bmatrix} \\ \mathbf{f_a}(\boldsymbol{\eta}, \phi(\boldsymbol{\eta})) \\ \\ \hline f_b(\boldsymbol{\eta}, \phi(\boldsymbol{\eta})) \end{bmatrix} + \begin{bmatrix} 0 \\ 0 \\ 0 \\ \hline g_b(\boldsymbol{\eta}, \phi(\boldsymbol{\eta})) \end{bmatrix} \tag{4.27}$$

$$\begin{bmatrix} \dot{\eta}_1 \\ \dot{\eta}_2 \\ \dot{\eta}_3 \\ \hline \dot{\xi} \end{bmatrix} = \begin{bmatrix} \frac{\cos\eta_1}{l}\xi - \eta_2 \\ \frac{-\sin\eta_1}{l}(\frac{\cos\eta_1}{l}\xi - \eta_2)\xi + \frac{\cos\eta_1}{l} f_4(\boldsymbol{\eta}, \xi) - f_3(\boldsymbol{\eta}, \xi) \\ \xi \\ \hline f_4(\boldsymbol{\eta}, \xi) \end{bmatrix} \begin{bmatrix} 0 \\ 0 \\ 0 \\ \hline g_4(\boldsymbol{\eta}, \xi) \end{bmatrix} \quad , \tag{4.28}$$

where,

$$\begin{aligned} f_3(\boldsymbol{\eta}, \xi) = & \frac{1}{l^2 m(M + m - m\cos^2\eta_1)} \left[(M+m) b_{p,v} \left(\eta_2 - \frac{\cos\eta_1 \xi}{l} \right) + \right. \\ & + (M+m) b_{p,c} \tanh\left(\mathrm{k_{tanh}} \left(\eta_2 - \frac{\cos\eta_1\xi}{l} \right) \right) + m^2 g l \sin\eta_1 - b_{c,c} m l \tanh(\mathrm{k_{tanh}}\xi) \cos\eta_1 - \\ & \left. - m^2 l^2 \cos\eta_1 \sin\eta_1 \left(\eta_2 - \frac{\xi\cos\eta_1}{l} \right)^2 + Mglm\sin\eta_1 - b_{c,v} m l \xi \cos\eta_1 \right] \end{aligned} \tag{4.29}$$

$$\begin{aligned} f_4(\boldsymbol{\eta}, \xi) = & -\frac{1}{l(M + m - m\cos^2\eta_1)} \left[b_{c,v} l \xi - b_{p,v} \cos\eta_1 \left(\eta_2 - \frac{\cos\eta_1\xi}{l} \right) + b_{c,c} l \tanh(\mathrm{k_{tanh}}\xi) - \right. \\ & - b_{p,c} \tanh\left(\mathrm{k_{tanh}} \left(\eta_2 - \frac{\cos\eta_1\xi}{l} \right) \right) \cos\eta_1 + \\ & \left. + l^2 m \sin\eta_1 \left(\eta_2 - \frac{\xi\cos\eta_1}{l} \right)^2 - mgl\cos\eta_1\sin\eta_1 \right] \end{aligned} \tag{4.30}$$

$$g_4(\boldsymbol{\eta}, \xi) = \frac{1}{M + m - m\cos^2\eta_1} \quad . \tag{4.31}$$

With the system on regular form, design is proceeded by choosing a sliding manifold,

$$s = \xi - \phi(\boldsymbol{\eta}) \quad , \tag{4.32}$$

where $\phi(\boldsymbol{\eta})$ is to be designed. If s is zero then $\xi = \phi(\boldsymbol{\eta})$, such that,

$$\dot{\boldsymbol{\eta}} = f_a(\boldsymbol{\eta}, \phi(\boldsymbol{\eta})) \quad , \tag{4.33}$$

is the reduced-order system with $\phi(\boldsymbol{\eta})$ as control input. It is then sought to design $\phi(\boldsymbol{\eta})$ such that Equation 4.33 is asymptotically stable at its origin.
To that end, the reduced-order system is linearized,

$$A = \left. \frac{\partial \dot{\boldsymbol{\eta}}}{\partial \boldsymbol{\eta}} \right|_{\substack{\boldsymbol{\eta}=\mathbf{0} \\ \xi=0 \\ \mathrm{k_{tanh}}=1}} = \begin{bmatrix} 0 & -1 & 0 \\ -\frac{g}{l} & \frac{-b_{p,v}}{l^2 m} & 0 \\ 0 & 0 & 0 \end{bmatrix} \quad , \quad B = \left. \frac{\partial \dot{\boldsymbol{\eta}}}{\partial \xi} \right|_{\substack{\boldsymbol{\eta}=\mathbf{0} \\ \xi=0 \\ \mathrm{k_{tanh}}=1}} = \begin{bmatrix} \frac{1}{l} \\ \frac{b_{p,v} + b_{p,c} l}{l^3 m} \\ 1 \end{bmatrix} \quad . \tag{4.34}$$

Checking for controllability,

$$\operatorname{rank}(\mathcal{C}) = \operatorname{rank}([\ B \quad AB \quad A^2B\ ]) = 3 \quad , \tag{4.35}$$

and since the controllability matrix, $\mathcal{C}$, has full rank, the linearized system is controllable. A state feedback controller is designed for the linearized reduced-order system,

$$\phi(\boldsymbol{\eta}) = -\mathbf{k}\boldsymbol{\eta} \quad . \tag{4.36}$$

The poles are placed in $\mathbf{p} = [\ -4 \quad -6 \quad -7\ ]$ using matlab *place()*-command to obtain the gains, $\mathbf{k} = [\ 7.2025 \quad -1.2930 \quad -5.4218\ ]$. Simulations of the controlled reduced-order system are run for both the linearized and the nonlinear system, see Figure 4.1.

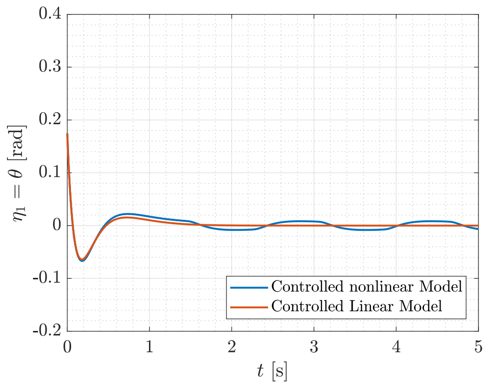

(a) The angle reaches zero with small oscillations in the nonlinear simulation.

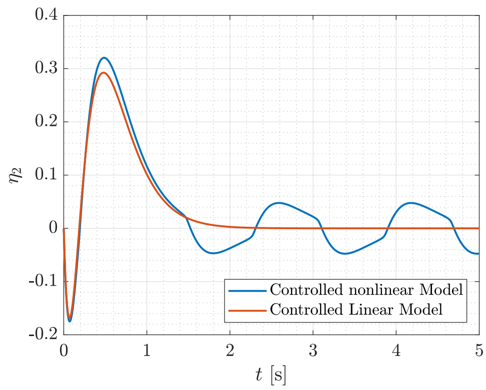

(b) Large oscillations occur in the nonlinear simulation. This parameter does not directly have a physical interpretation.

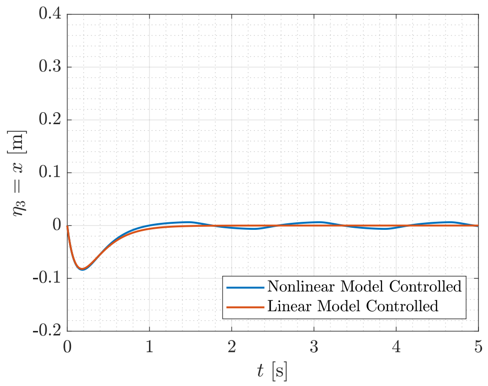

(c) The cart position reaches zero with small oscillations in the nonlinear simulation.

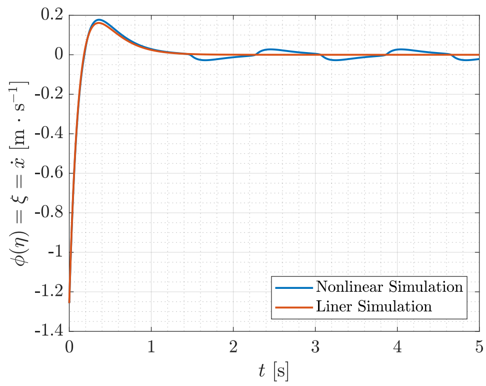

(d) The tendency to oscillations in the nonlinear simulation also appears in the control signal for the reduced-order system.

Figure 4.1: Nonlinear and linear simulation of the state feedback control designed for the linearized reduced-order system.

The reduced-order system is stabilized under the assumption that s is zero. Thus, the design of u is concerned with bringing s to zero.

Theorem 4.0.1 (Lyapunov Stability Theorem) *Consider the autonomous system,* $f(\mathbf{x}) = \dot{\mathbf{x}}$*, where* $f : \mathbb{D} \to \mathbb{R}^n$ *is locally Lipschitz and* $\mathbf{x} = \mathbf{0}$ *is an equilibrium point. Then if* $\exists\, V : \mathbb{D} \to \mathbb{R}$ *and*

1. $V(\mathbf{x})$ *is* C^1
2. $V(\mathbf{x}) > 0 \;\forall\; \mathbf{x} \in \mathbb{D}\backslash 0$ *and* $V(\mathbf{0}) = 0$
3. $\dot{V}(\mathbf{x}) \leq 0$ *in* $\mathbb{D}$

then $\mathbf{x} = \mathbf{0}$ *is stable. Further, if,*

$$\dot{V}(\mathbf{x}) < 0 \text{ in } \mathbb{D}\backslash 0 \quad ,$$

then $\mathbf{x} = \mathbf{0}$ *is asymptotically stable [15].*

A Lyapunov function candidate is proposed,

$$V(\boldsymbol{\eta}, \xi) = \tfrac{1}{2}s^2 \quad , \tag{4.37}$$

where $s = \xi - \mathbf{k}\boldsymbol{\eta}$ hence,

$$V = \tfrac{1}{2}(\xi - \mathbf{k}\boldsymbol{\eta})^2 \tag{4.38}$$

$$V = \tfrac{1}{2}(\xi^2 + (\mathbf{k}\boldsymbol{\eta})^2) - \xi\mathbf{k}\boldsymbol{\eta} \tag{4.39}$$

$$\begin{aligned} V = {} & \tfrac{1}{2}(\xi^2 + k_1^2\eta_1^2 + k_2^2\eta_2^2 + k_3^2\eta_3^2) + k_1k_2\eta_1\eta_2 + k_1k_3\eta_1\eta_3 + k_2k_3\eta_2\eta_3 - \\ & - \xi(k_1\eta_1 + k_2\eta_2 + k_3\eta_3) \quad . \end{aligned} \tag{4.40}$$

The partial derivatives are,

$$\frac{\partial V}{\partial \xi} = \xi - \mathbf{k}\boldsymbol{\eta} \tag{4.41}$$

$$\frac{\partial V}{\partial \eta_1} = k_1^2\eta_1 + k_1k_2\eta_2 + k_1k_3\eta_3 - k_1\xi \quad , \tag{4.42}$$

and similar results to Equation 4.42 are obtained for the partial derivatives with respect to η_2 and η_3. Since all four partial derivatives are C^0 then V is C^1 in the entire $\mathbb{R}^4$, thus satisfying the first condition of the Lyapunov Stability Theorem 4.0.1. Further, from Equation 4.38, it is clear that V is positive definite in the entire state space without zero and zero in the origin, thus also satisfying the second condition.

To assess the third condition of Theorem 4.0.1, the derivative of the Lyapunov function candidate is found along trajectories of the system,

$$\dot{V} = s\dot{s} \tag{4.43}$$

$$\dot{V} = s(\dot{\xi} + \mathbf{k}\dot{\boldsymbol{\eta}}) \tag{4.44}$$

$$\dot{V} = s(f_b(\boldsymbol{\eta}, \xi) + g_b(\boldsymbol{\eta}, \xi)u + \mathbf{k}f_a(\boldsymbol{\eta}, \xi)) \tag{4.45}$$

$$\dot{V} = (\mathbf{k}f_a + f_b)s + g_b s u \tag{4.46}$$

$$\dot{V} = g_b s(\mathbf{k}f_a + f_b)g_b^{-1} + g_b s u \tag{4.47}$$

$$\dot{V} \leq g_b|s|\,|\mathbf{k}f_a + f_b|\,g_b^{-1} + g_b s u \quad . \tag{4.48}$$

This leads to the design of u which is chosen such that the third condition of Theorem 4.0.1 is satisfied,

$$u = -\mathrm{sgn}(s)\beta(\boldsymbol{\eta},\xi)g_b^{-1}(\boldsymbol{\eta},\xi) \quad \text{where,} \quad \beta(\boldsymbol{\eta},\xi) = \varrho(\boldsymbol{\eta},\xi) + \beta_0 \tag{4.49}$$

$$\varrho(\boldsymbol{\eta},\xi) = |\mathbf{k}f_a + f_b| \quad , \tag{4.50}$$

and $\beta_0 > 0$ is a tuning parameter allowing $\dot{V}$ to be positive definite, thereby guaranteeing asymptotic stability of the origin by Theorem 4.0.1,

$$\dot{V} < g_b|s|\,|\mathbf{k}f_a + f_b|\,g_b^{-1} - g_b\,\mathrm{sgn}(s)s\,|\mathbf{k}f_a + f_b + \beta_0|\,g_b^{-1} \quad . \tag{4.51}$$

For implementation, the discontinuity introduced by the sign-function in the control law is cause for excessive switching and chattering due to delays in the real system. To circumvent this issue, a saturation function with a steep slope, $1/\varepsilon$, is used to approximate the sign-function,

$$\mathrm{sat}\,(s/\varepsilon) = \begin{cases} s/\varepsilon & |s/\varepsilon| \leq 1 \\ \mathrm{sgn}\,(s) & |s/\varepsilon| > 1 \end{cases} \quad , \tag{4.52}$$

hence,

$$u = -\mathrm{sat}(s/\varepsilon)\beta(\boldsymbol{\eta},\xi)g_b^{-1}(\boldsymbol{\eta},\xi) \quad . \tag{4.53}$$

A simulation of the design is shown in Figure 4.2 and 4.3, starting from an initial angle of $0.1\,\mathrm{rad}\cdot\mathrm{s}^{-1}$. Both the angle and cart position are brought to zero. The small oscillations are thought to origin from the linear part of the design, where oscillations were observed in the simulation of the nonlinear reduced order system with linear control, see Figure 4.1.

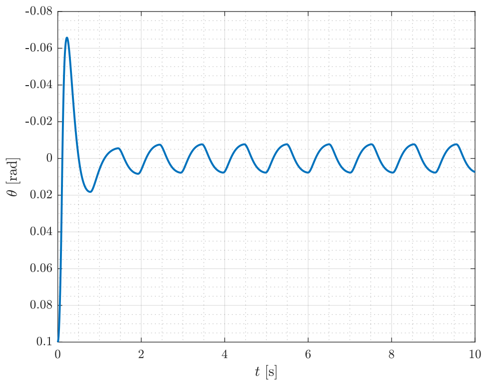

Figure 4.2: A simulation of the sliding mode design starting form an initial angle of $0.1\,\mathrm{rad}\cdot\mathrm{s}^{-1}$ at zero angular velocity. The angle is maintained around zero with small oscillation.

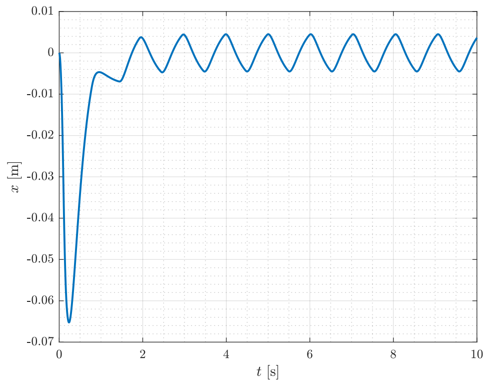

Figure 4.3: The cart position successfully returns to zero with small oscillations after the pendulum angle is brought to zero.

To achieve this behavior from relatively wide catch angle, a large peak occurs in the armature current, see Figure 4.4. However, with the short duration of the peak, this is not considered a problem. If it is desired to bring down the peak current, the sliding mode controller could simply be activated at a narrower angle.

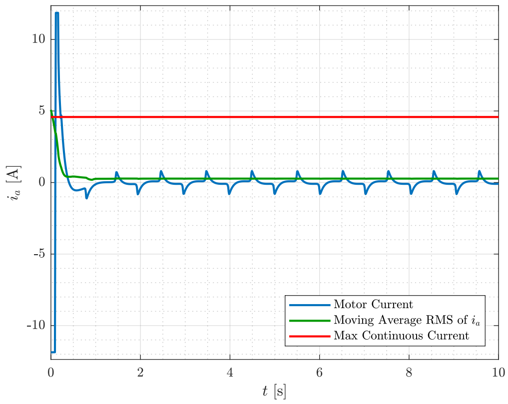

Figure 4.4: The control signal from the simulation in Figure 4.2 and 4.3. The peak current is rather large, which is to be expected given the relatively wide initial angle. It is not considered to be a problem, since the large current is only maintained for a short duration.

Finally the swing-up controller and the sliding mode controller are simulated in concert, where the sliding mode controller is activated at a catch angle of 0.1 rad. The result is seen in Figure 4.5 and Figure 4.6, where the swing-up controller brings the angle below the catch angle in seven swings, after which the system is stabilized in zero by the sliding mode controller.

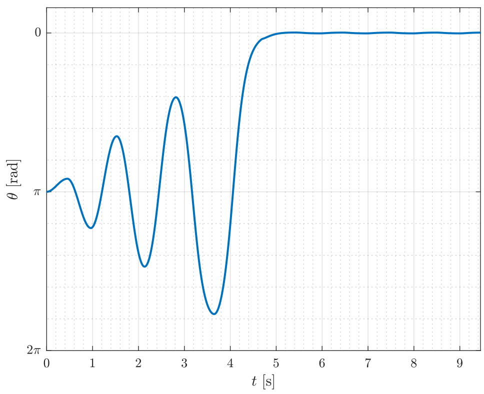

Figure 4.5: Simulation of the swing-up controller using sliding mode to catch the pendulum when the angle reaches below 0.1 rad.

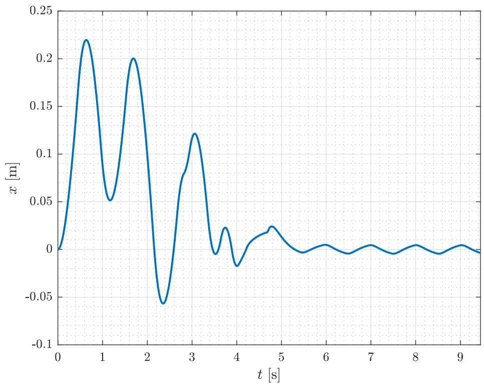

Figure 4.6: The cart position successfully returns to zero after the pendulum angle is stabilized at zero.

The needed actuation signal is seen in Figure 4.7 and though some peaks occur, the RMS stays below the rated continuous current limit of the motor.

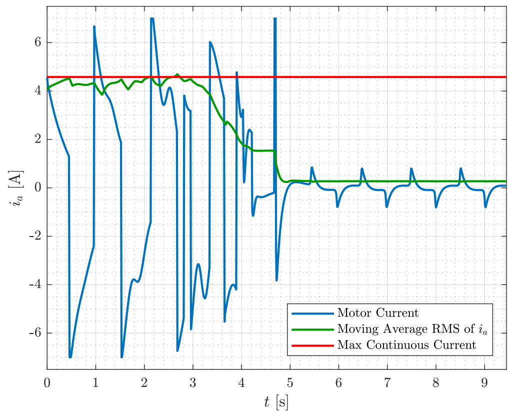

Figure 4.7: Control signal from the simulation in Figure 4.5 and 4.6. Again large peaks occur in the armature current, however, only for short durations and with the RMS staying below the rated continuous current limit.

The system was first transformed into *regular form* after which the reduced order system was stabilized using linearization and linear state feedback. Some small oscillations were observed in the nonlinear simulation of the controlled reduced order system. The sliding mode design was proceeded from there based on Lyapunov stability criteria, and the final control law was simulated stabilizing the system also in concert with the swing-up controller.
This concludes the stabilization design and carries into the final two chapters of *Part 1* where considerations in implementation are presented along with the final test results from the cart pendulum system setup.

5 | Implementation

To implement the control designs discussed here in *Part 1* it is necessary to estimate some parameters, compensate for any friction between the cart and the rail and filter the measurements obtained from the system. Such considerations, estimations and designs are discussed in this section.

5.1 Cart Friction and Mass Estimation

The control designs are carried out under the assumption that there is no friction between the cart and the rail. It turns out that this friction is rather complex and also depend on position and direction of the cart in addition to its velocity, this issue was also found by previous project groups [7].
To accommodate the no cart friction assumption, a feed forward friction compensator is designed. The idea is to simply counter the predicted friction at any given time directly in the control signal.

Since the friction depends on the cart position, the estimation must be done locally for each position on the rail. To do so, the pendulum masses are removed, the rods strapped to the cart to limit dynamics and the cart is made to oscillate around each centimeter of the rail. Each test is sustained for 20 s and repeated for each centimeter, resulting in a total of 68 tests. This is the largest possible range for the test while avoiding impact at the ends of the rail. Each test spans on average 2.68 cm creating some overlap between tests. The reduced dynamics used for the estimation are given by,

$$(M+m)\ddot{x} = u - b_{c,v}\dot{x} - \tanh(\mathrm{k}_{\tanh}\dot{x})b_{c,c} \quad . \tag{5.1}$$

The optimization fitting tool, Senstools [16], is used to estimate the model parameters. Since the mass is unknown it is also included for estimation. The mass is estimated to be 6.28 kg. With more parameters more manual tuning is required in order to start close enough for the optimization algorithm to converge. To reduce the number of parameters as much as possible, once estimated, the mass is fixed as part of the model. The remaining three parameters are viscous friction and coulomb friction for negative and positive velocities. After some trail and error it is concluded that the viscous friction is negligible compared to the coulomb frictions finally leaving only two parameters.
To make the estimations converge without too much manual tuning only part of each test is fitted, see Figure 5.1. The time window is moved, and the estimation is run again. The window is moved 34 times resulting in $34 \cdot 68 = 2312$ estimations in total. Every time the test window is moved, the next estimate is started with the results of the previous estimate as its initial values.

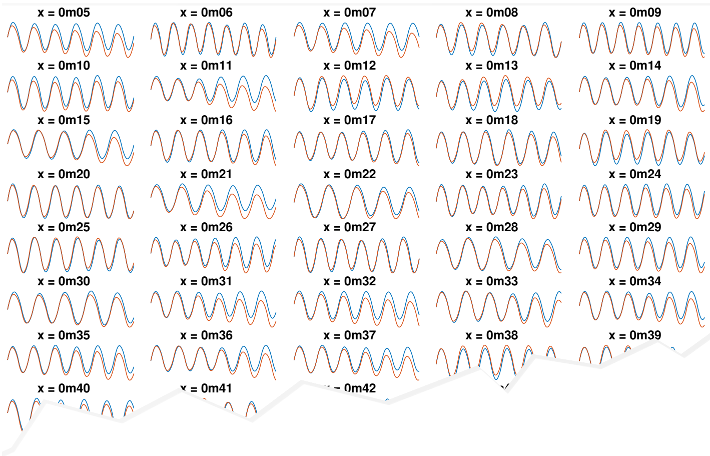

Figure 5.1: A snippet of the estimation of cart Coulomb friction. Each title shows where on the rail the test is done. This is one iteration of 34 moving over the 20 s tests.

To include as much data as possible, the estimate is repeated across the data for each test, resulting in 34 results for each position. The error norm is saved for all estimations, see Figure 5.3, and a weighed average using the error norm as weights is made for each position on the rail resulting in Figure 5.2.

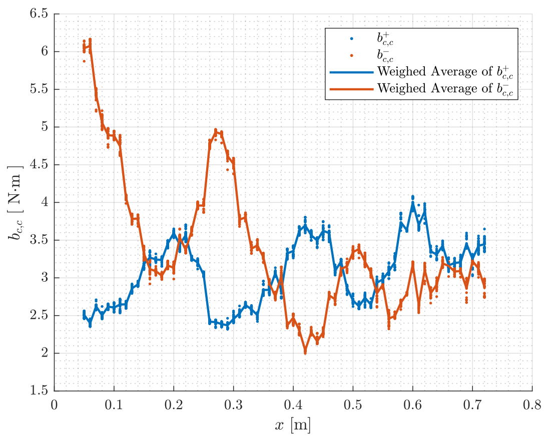

Figure 5.2: Results of the estimations, where the scattered points are all estimates and the lines are the weighed averages using the error norm of each estimate as weights.

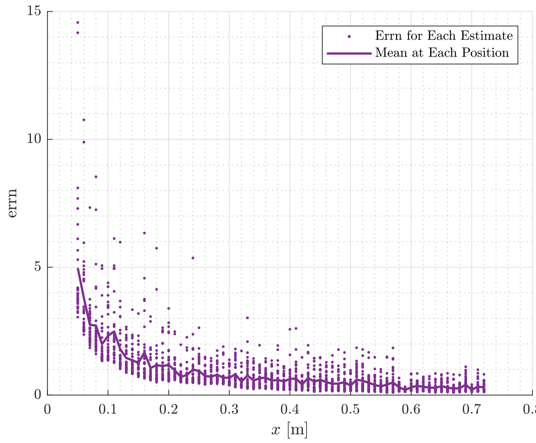

Figure 5.3: This shows the error norms for all estimates. There is a clear tendency to worse fits at the left end of the rail. The reason is unknown.

The estimations are worse near the left of the rail, see Figure 5.3. The cause for this is not known, however it is considered less important as the compensation is more critical near the middle of the rail where the pendulum is balanced.

The result in Figure 5.2 contains some undesired discontinuities. To solve this problem the resulting mean curves are up-sampled by linear interpolation, smoothed and finally down-sampled to obtain the smoothed result in Figure 5.4.

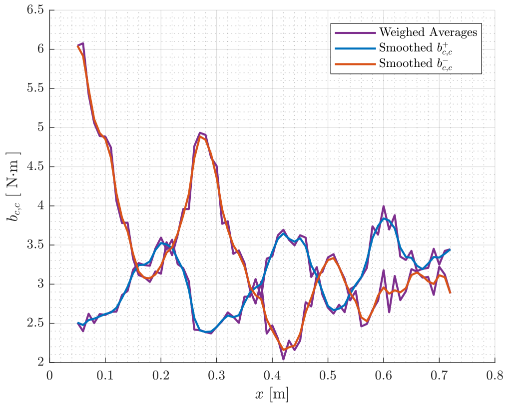

Figure 5.4: This is the final result of the estimation, which is up-sampled, smoothed and finally down-sampled to produce the values for implementation in lookup-table.

The result is implemented as lookup tables along with a linear interpolation function to avoid discontinuities between table entries. This determines the cart Coulomb friction based on velocity, direction and position, which is then added to the control signal to counter the friction therm in the dynamics.

5.2 Pendulum Friction

With the cart mass estimated and its friction handled by friction compensation, the remaining estimate is pendulum friction. Again Senstools is used along with a reduced model of the pendulum,

$$ml^2\ddot{\theta} = mgl\sin\theta - b_{p,v}\dot{\theta} - \tanh(k_{tanh}\dot{\theta})b_{p,c} \quad . \tag{5.2}$$

This model assumes there is no cart, so for the test, the cart is fixed to the rail. The result of the test and estimation is seen in Figure 5.5.

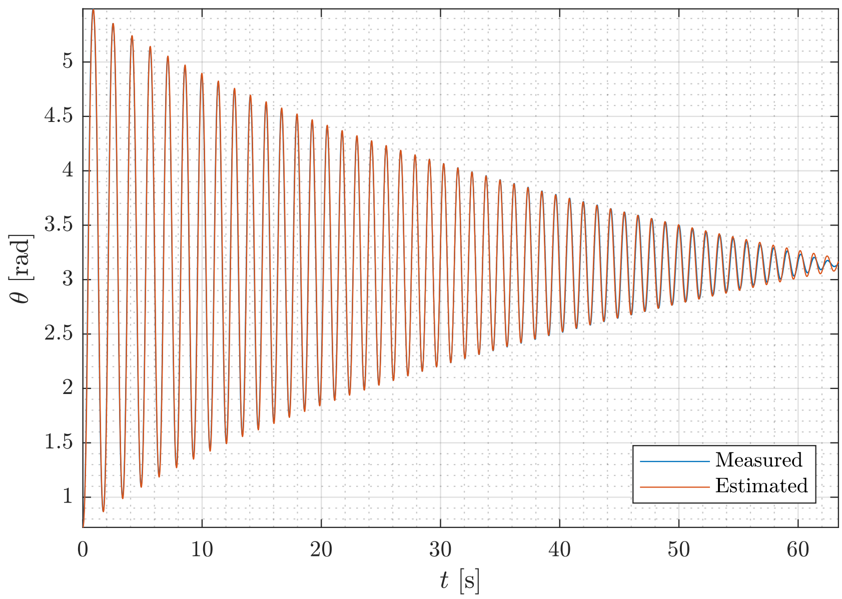

Figure 5.5: The fit resulting in the estimations of the pendulum friction.

To obtain a good fit, 22.5 g is added to the measured mass and 0.66 cm is subtracted from the measured length of the rod. This is presumed to be reasonable, since the rod is otherwise assumed to be massless which is not the case. The error in the assumption would move the mass center closer to the pivot point, thus reducing the effective length of the rod and adding some mass to the weight, corresponding to the adjustments. The pendulum Coulomb friction, $b_{p,c}$, is estimated to $4.1 \times 10^{-3}\,\mathrm{N \cdot m}$ and the viscous friction, $b_{p,v}$, to $0.5 \times 10^{-3}\,\mathrm{N \cdot m \cdot s}$.

5.3 MA Filter Design

The measurements in the system are the position, x, of the cart and the angle, θ, of the pendulum. Thus, the last two states, $\dot{x}$ and $\dot{\theta}$, must be estimated for the implementation. To that end, a numerical differentiation is applied to the position measurements in order to obtain the velocities,

$$\dot{x} = \frac{x_0 - x_{-1}}{T_s} \quad , \tag{5.3}$$

where T_s is the sample time and x_0 and x_{-1} are the two latest samples. However, this approach causes noise in the velocities. Thus, an MA (Moving Average) filter is designed to smooth the signal,

$$\dot{x}_{est} = \frac{1}{N} \sum_{i=1-N}^{0} \dot{x}_i \quad , \tag{5.4}$$

where $\dot{x}_0$ is the numerical differentiation based on the two latest measurements, x_{est} is the filtered value and N is the window size of the filter. In Figure 5.6 and 5.7 the MA filter is applied to the result of the numerical differentiation with two different window sizes. Since the interest here is quality of the signal, the following plots are not linked in time, but rather showing the signals where the filter characteristics shows clearly.

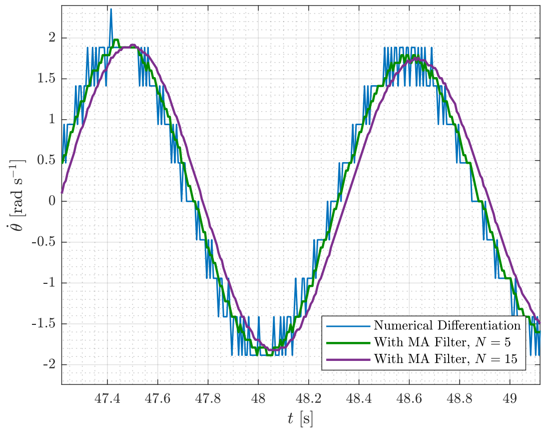

Figure 5.6: The result of applying the MA filter to the numerical differentiation of θ with two window sizes. For $N = 5$ a lot of noise is still in the signal, however, though $N = 15$ removes more noise it also introduces unwanted delay.

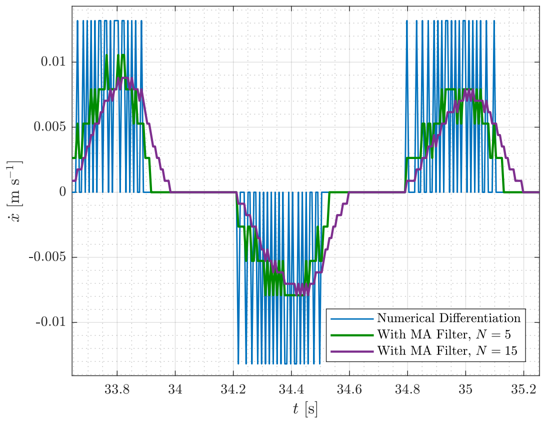

Figure 5.7: For $\dot{x}$ the same result is observed, but since the signal is smaller relative to the noise, it more clearly shows the noise issue of the small window size.

The filter is implemented using a ring-buffer to minimize computation time and different window sizes are tested. Minimizing delay of the filter turns out to be more critical than further noise reduction, so a window size of five is chosen. The result of the implemented MA filter is shown in Figure 5.8 and 5.9.

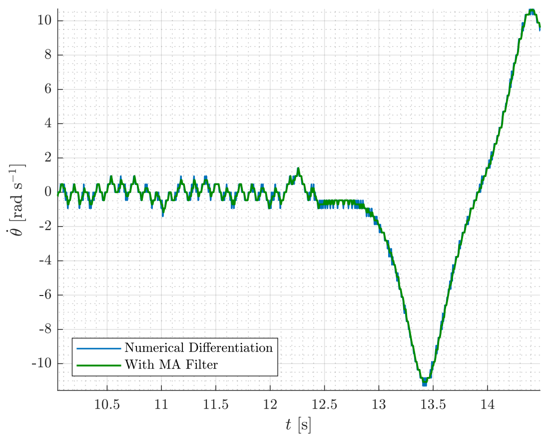

Figure 5.8: The resulting implementation of the MA filter with $N = 5$ for estimation of $\dot{\theta}$.

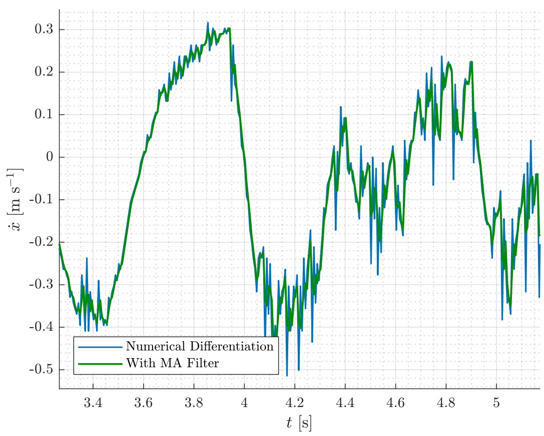

Figure 5.9: The implemented MA filter with $N = 5$ for estimation of $\dot{x}$.

Though the MA filter still lets a lot of noise through, the design does suppress large jumps in the velocity with very minimal delay.

This filter is only used in the swing-up sequence, an extended Kalman filter (EKF) implemented by a previous project group, [7], is used for the catch sequence as the switching nature of a sliding mode controller would cause oscillations with high noise levels around zero.

6 | Results

Here the results of the implemented control strategies developed in *Part 1* are presented. Firstly, the swing-up controller is approaching a heteroclinic orbit after seven swings, see Figure 6.1 and 6.2, same as achieved in simulation when accounting for actuation limitations.

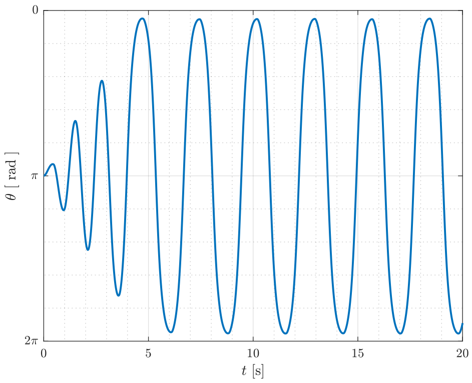

Figure 6.1: The swing-up controller approaches the equilibrium and almost reaches the heteroclinic orbit.

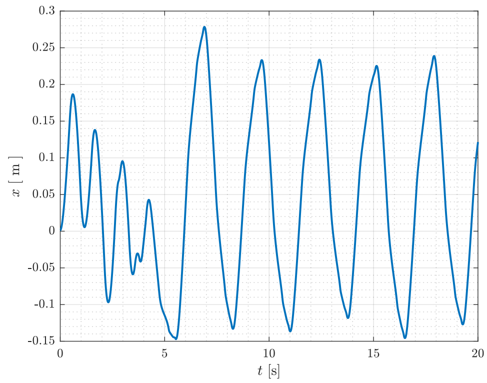

Figure 6.2: Though the cart oscillates more than in the simulation, it stays around zero and within the rail limits during the swing-up sequence.

The controller does fall slightly short of reaching the heteroclinic orbit which is also seen in Figure 6.4. The energy reference in Figure 6.3 reaches zero near the equilibrium points, but must be very slightly below zero when the angular velocity is zero, as otherwise the pendulum would reach equilibrium exactly.

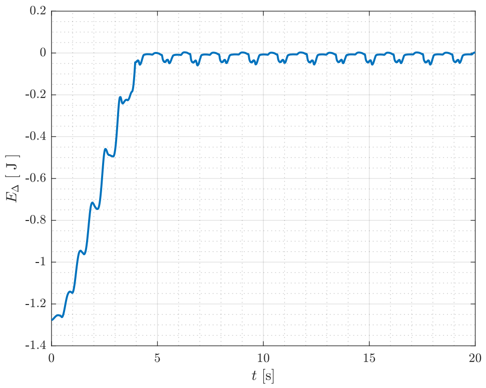

Figure 6.3: From the test in Figure 6.1 and 6.2 the energy reference is reached.

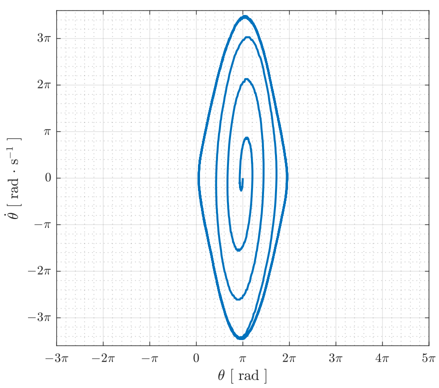

Figure 6.4: The pendulum almost reaches a heteroclinic orbit.

It is possible to gain closer proximity to the equilibrium point by increasing the energy reference. In Figure 6.5 and 6.6 the energy reference is increased by 0.08 J to reach heteroclinic orbit.

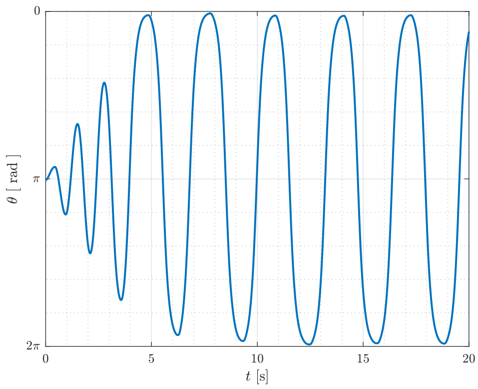

Figure 6.5: The swing-up controller approaches the equilibrium and eventually reaches the heteroclinic orbit.

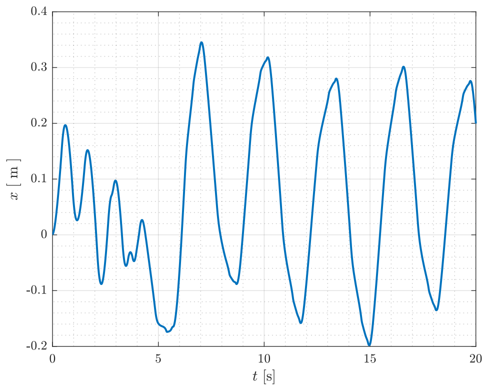

Figure 6.6: The cart does not approach zero position as much as it did in simulation. It does however stay within the constraints of the physical system, which is the main objective of the added position control for the swing-up sequence.

In Figure 6.7 the energy reference is slightly lifted causing a near perfect heteroclinic orbit in Figure 6.8.

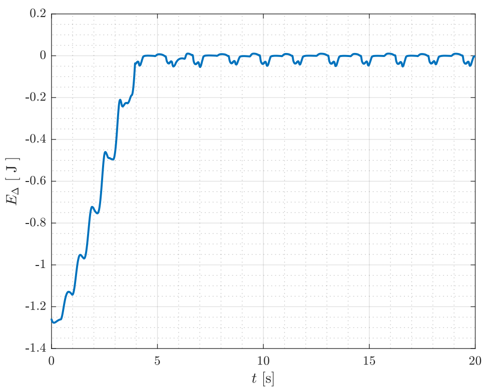

Figure 6.7: From the test in Figure 6.5 and 6.6 where the energy reference is raised by 0.08 J to get closer to the equilibrium point.

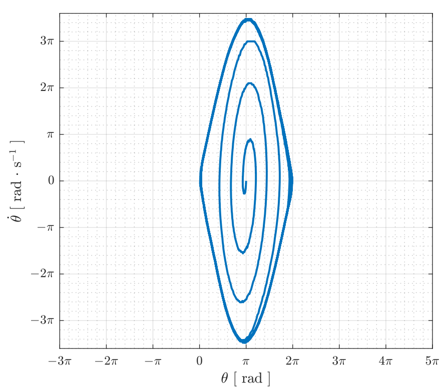

Figure 6.8: Near perfect heteroclinic orbit is reached due to the slight increase of the energy reference.

If the model and friction compensation was ideal, no energy offset would be needed, so if a high value was needed to approach equilibrium it might be worth to revisit this part of the design process.

Figure 6.9 shows the armature current of the motor used to achieve the swing-up behavior with the added energy reference. Though some peaks are present in the current signal, the

RMS value does not exceed the continuous current specification of the motor for extended periods of time.

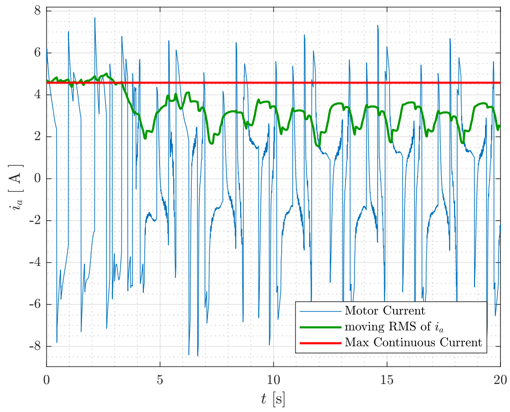

Figure 6.9: The RMS of the armature current is withing respectable levels of the specified contentious current limit of the motor.

A test of the implemented sliding mode controller is seen in Figure 6.10 and 6.11 where the angle reaches zero.

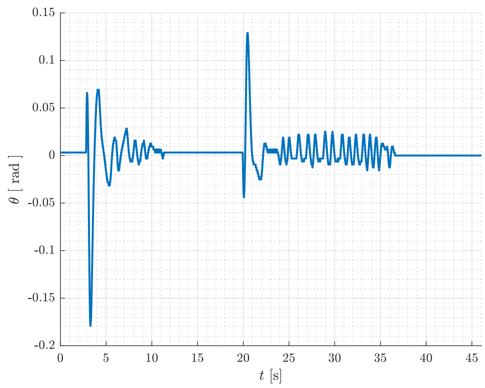

Figure 6.10: Test of sliding mode controller starting at zero. The controller is subjected to two disturbances after which it rebalances successfully bringing the angle back to zero.

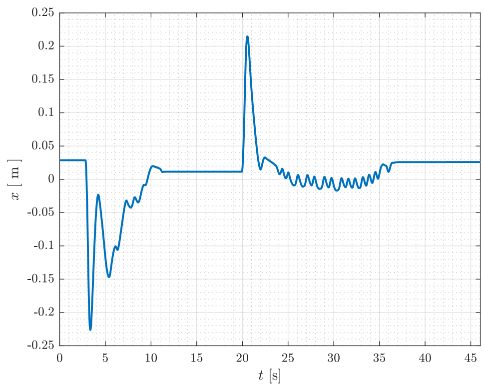

Figure 6.11: The cart returns approaches zero once the pendulum is rebalanced.

In the last part, after the 35 s mark, an offset in x is observed, this could be contributed to unmodeled friction keeping the control from exceeding the force of friction. The control signal is shown in Figure 6.12 where it does have a constant offset after the 35 s mark, supporting the hypothesis. However, the offset is also seen in the other stabilized regions of the test, where the control signal goes to zero. So while the first hypothesis might in part be true, something else is at least contributing to the problem, otherwise the control would still show an offset where the cart position does.

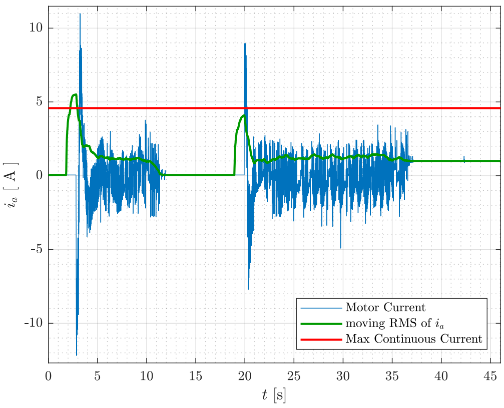

Figure 6.12: The armature current has an offset after 35 s which matches an offset in the position, however, around 15 s the same offset is seen in position with no offset in armature current.

When testing, an other problem relating to the position of the cart was observed. In Figure 6.13 the pendulum is only pushed once in the start of the test. The cart spontaneously diverges from zero position before correcting and re-stabilizing. When this happens, the angular velocity should not increase much, as seen by the FIR filter, which by nature does not introduce bias, however, the EKF shows an increase in angular velocity.

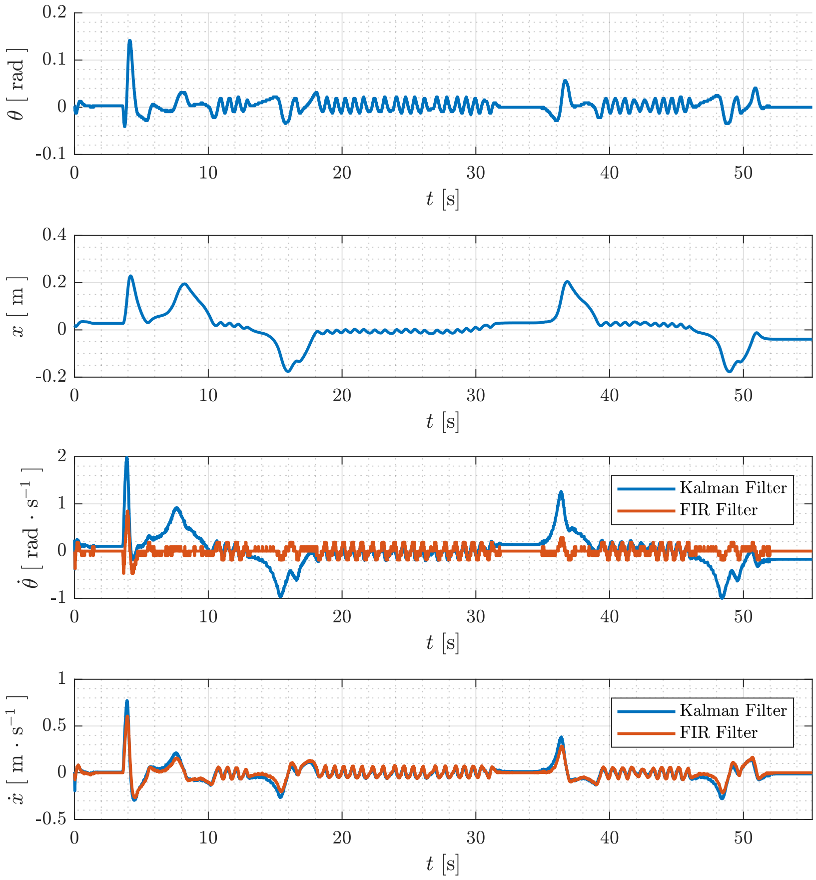

Figure 6.13: The system is perturbed about 4 s into the test, remaining disturbances are caused by a problem presumed to arise between friction compensation and the EKF.

If the friction compensation is too large, this could cause the cart to move away from equilibrium, and in that event, the EKF which is based on a system model, would get data which does not confine to the model, which might lead to a wrong estimation of the angular velocity, which would then amplify the problem.

When finally combining the two control strategies it is advantageous for the catch controller if the swing-up controller is designed to provide a bit of entry velocity at equilibrium. This makes for a more robust swing-up controller, in that, it always reaches the equilibrium in the same number of swings for every test. This means that the swing-up controller would overshoot without a catch controller. However, as the catch controller is enabled close to equilibrium, this helps the sliding mode controller by providing entry velocity at the maximum catch angle.
It is further noted that smaller catch angles causes less aggressive actuation of the sliding mode controller. After entering sliding mode the catch angle is increased, such that it stays in sliding mode unless the pendulum exceeds the maximum angle at which sliding mode can successfully re-stabilize the system. When this angle is exceeded, the swing-up controller is enabled and the catch angle is again reduced. As in simulation, a wrapped version of the angle is created such that the pendulum is always at zero when in upright position, this representation is only used by sliding mode.
Results of a test of the full implementation of the two controllers is shown in Figure 6.14 and 6.15.

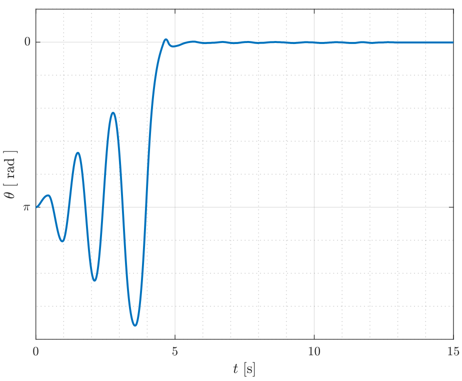

Figure 6.14: Test of the final design of swing-up with the higher energy reference and sliding mode controller successfully catching the pendulum after seven swings.

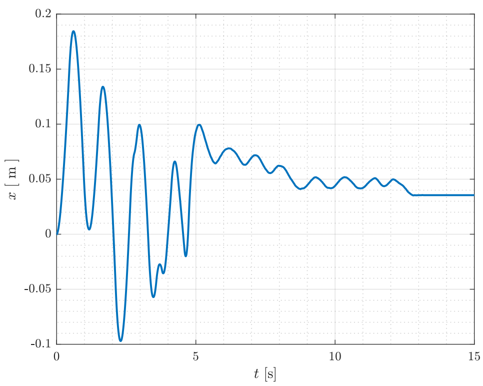

Figure 6.15: The cart keeps around zero on the rail, especially after the pendulum angle is controlled to zero.

The swing-up controller successfully hands over to sliding mode after seven swings and the sliding mode controller stabilizes the system in zero with some offset in the cart position. The moving average RMS of the actuation current briefly exceeds the continuous current rating of the motor when sliding mode catches the pendulum. As this is not happening over a prolonged period, it is not thought to be a problem,

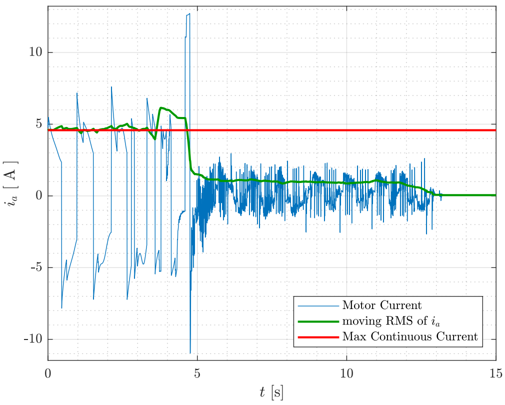

Figure 6.16: Armature current of the finished control system. It only briefly exceeds the motor specifications when the sliding mode controller takes over.

Three energy based swing-up designs were investigated, the sat-based version was chosen, a cart position controller was added and finally a stabilizing sliding mode controller was designed to catch the pendulum in equilibrium. The designs were successfully implemented and tested on the system setup concluding *Part 1* of this thesis.

Part II

Twin Pendulum

7 | System and Model

The cart pendulum system from *Part 1* is used again. However, here in *Part 2* an additional pendulum is mounted on the cart. The modification is discussed and a model for the changed system is developed in this chapter. The remaining of *Part 2* is concerned with estimating parameters, developing a state estimator, designing a swing-up controller and ultimately stabilizing the two pendulums in upright position.

7.1 System Addition

In Figure 7.1 the setup from *Part 1* is shown with the added pendulum. The new pendulum is mounted on a new motor (not directly visible in the figure), a brushed Maxon 370356 DC motor [1], same as for the first pendulum. The motor is not in use for this project and only acts as a joint with a HEDS 5540 optical quadrature encoder [2].

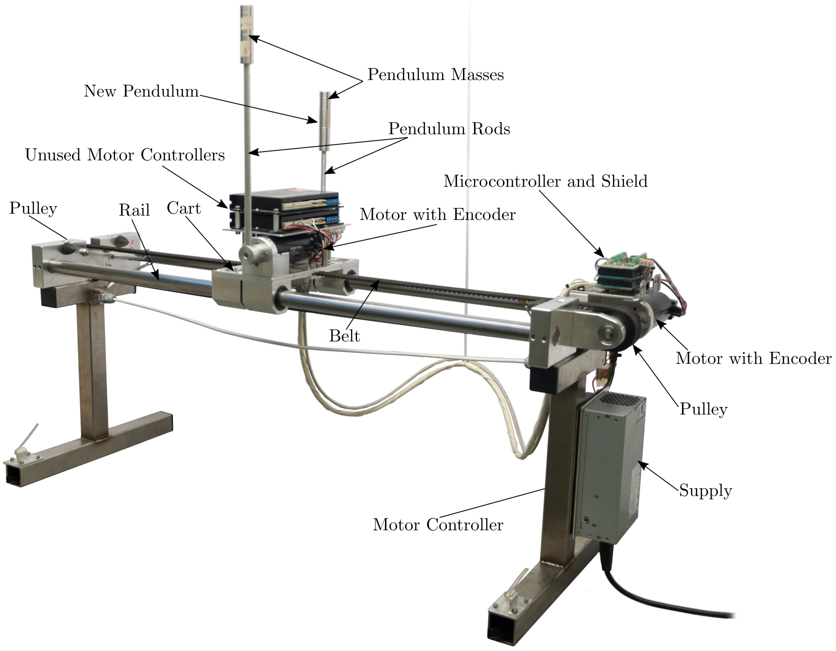

Figure 7.1: The setup form *Part 1* with a new pendulum attached on the back side of the cart. The motor controller in use is not directly visible here as it is mounted behind the supply.

The added pendulum measures 20 cm from pivot point to geometrical center of the 251 g weight at its end. The friction parameters are estimated again using Senstools, [16], and with the same reduced pendulum model as in *Part 1*.
Same as for the first pendulum, the mass is increased to obtain a good fit. In this case the pendulum mass is increased by 13.2 g, less than for the first pendulum, which makes sense since the added pendulum is shorter thus adding less mass to the system. For the first pendulum the length was decreased by 0.66 cm, while for the new pendulum the

measured length is used. Though the mass center should move towards the rod, it being shorter and with more mass at the end than the first pendulum, it makes sense that the mass center is moved so little for the new pendulum that the effect becomes negligible. Figure 7.2 shows the result of the estimation.

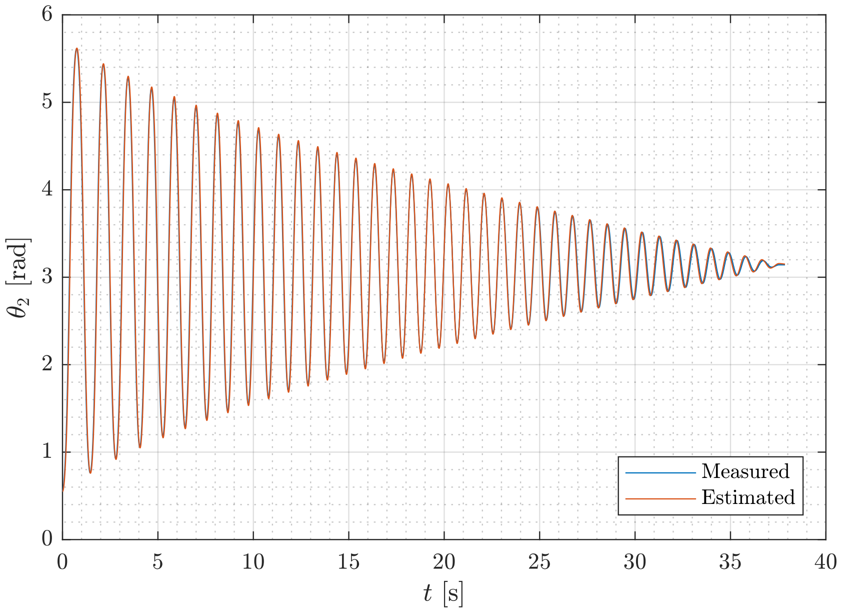

Figure 7.2: The fit resulting in the estimations of the new second pendulum friction, where θ_2 is the new pendulum angle.

In Table 7.1 all parameters for the twin pendulum system are gathered and notation is introduced to accommodate the added pendulum.

Parameter	**Notation**	**Quantity**	**Unit**
Nominal current (max. continuous current)	I_{N}	4.58	A
Torque constant	τ_m	93.4×10^{-3}	$\mathrm{N \cdot m \cdot A^{-1}}$
Pendulum 1 Rod Length	$l1$	0.3169	m
Pendulum 2 Rod Length	$l2$	0.2000	m
Rail Length	l_r	0.89	m
Pulley Radius	r	0.028	m
Pendulum 1 Mass	$m1$	0.2235	kg
Pendulum 2 Mass	$m2$	0.2642	kg
Cart Mass	M	6.28	kg
Cart Coulomb Friction	$b_{c,c}$	$f(x, \dot{x})$	N
Cart Viscous Friction	$b_{c,v}$	0	$\mathrm{N \cdot m^{-1}\ s}$
Pendulum 1 Coulomb Friction	$b_{p1,c}$	4.1×10^{-3}	$\mathrm{N \cdot m}$
Pendulum 1 Viscous Friction	$b_{p1,v}$	0.5×10^{-3}	$\mathrm{N \cdot m \cdot s}$
Pendulum 2 Coulomb Friction	$b_{p2,c}$	5.7×10^{-3}	$\mathrm{N \cdot m}$
Pendulum 2 Viscous Friction	$b_{p2,v}$	0.1×10^{-3}	$\mathrm{N \cdot m \cdot s}$

Table 7.1: Table of all system parameters including the estimated parameters for the added second pendulum. Notice the updated notation where *pendulum 1* is the pendulum also used in *Part 1* and *pendulum 2* is the newly attached pendulum.

In practice the new pendulum and motor were added before estimations were made in *Part 1*. This means parameters remain unchanged between the two versions of the setup allowing demonstration of both with the minimal modification of adding or removing the second pendulum mass.

7.2 Model

To model the twin pendulum system, consider the excessive coordinate convention in Figure 7.3 along with the generalized coordinates in the mechanical drawing, Figure 7.4.

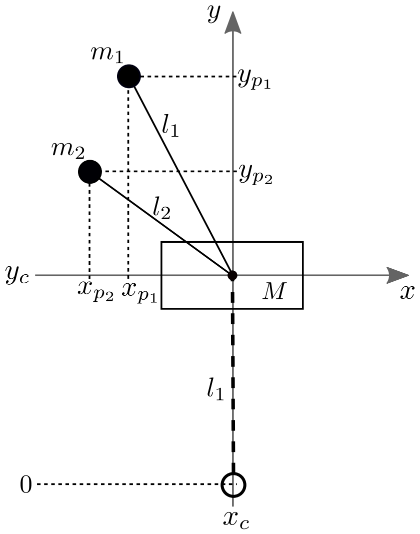

Figure 7.3: Twin pendulum system in excessive coordinates.

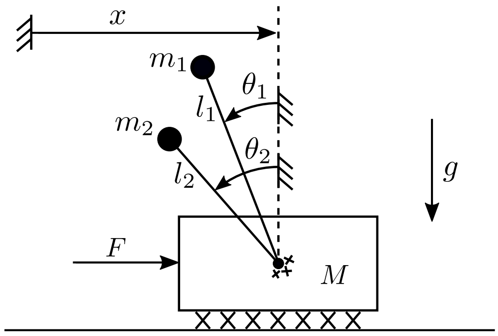

Figure 7.4: Mechanical drawing of the system with the added pendulum in generalized coordinates.

The energy method is applied. First the potential and kinetic energies, in therms of excessive coordinates, is found,

$$U = Mgy_c + m_1gy_{p_1} + m_2gy_{p_2} \tag{7.1}$$
$$T = \tfrac{1}{2}M\dot{x}_c^2 + \tfrac{1}{2}M\dot{y}_c^2 + \tfrac{1}{2}m_1\dot{x}_{p_1}^2 + \tfrac{1}{2}m_1\dot{y}_{p_1}^2 + \tfrac{1}{2}m_2\dot{x}_{p_2}^2 + \tfrac{1}{2}m_2\dot{y}_{p_2}^2 \quad . \tag{7.2}$$

The excessive coordinates and derivatives thereof are then expressed in therms of the generalized coordinates, using the conventions presented in Figure 7.3 and 7.4,

$$\begin{cases} x_c &= x \\ y_c &= l_1 \end{cases} \quad \begin{cases} x_{p_1} = x - l_1 \sin\theta_1 \\ y_{p_1} = l_1 + l_1\cos\theta_1 \end{cases} \quad \begin{cases} x_{p_2} = x - l_2\sin\theta_2 \\ y_{p_2} = l_1 + l_2\cos\theta_2 \end{cases} \tag{7.3}$$
$$\begin{cases} \dot{x}_c &= \dot{x} \\ \dot{y}_c &= 0 \end{cases} \quad \begin{cases} \dot{x}_{p_1} = \dot{x} - l_1\cos\theta_1\dot{\theta}_1 \\ \dot{y}_{p_1} = -l_1\sin\theta_1\dot{\theta}_1 \end{cases} \quad \begin{cases} \dot{x}_{p_2} = \dot{x} - l_2\cos\theta_2\dot{\theta}_2 \\ \dot{y}_{p_2} = -l_2\sin\theta_2\dot{\theta}_2 \end{cases} \quad . \tag{7.4}$$

Inserting Equation 7.3 and 7.4 into the energy equations, Equation 7.1 and 7.2, yields,

$$U = Mgl_1 + m_1g(l_1 + l_1\cos\theta_1) + m_2g(l_1 + l_2\cos\theta_2) \tag{7.5}$$
$$\begin{aligned} T = {} & \tfrac{1}{2}M\dot{x}^2 + \tfrac{1}{2}m_1(\dot{x} - l_1\cos\theta_1\dot{\theta}_1)^2 + \tfrac{1}{2}m_1(-l_1\sin\theta_1\dot{\theta}_1)^2 + \\ & + \tfrac{1}{2}m_2(\dot{x} - l_2\cos\theta_2\dot{\theta}_2)^2 + \tfrac{1}{2}m_2(-l_2\sin\theta_2\dot{\theta}_2)^2 \quad . \end{aligned} \tag{7.6}$$

Proceeding to compute the Lagrangian,

$$\mathcal{L} = T - U \tag{7.7}$$

$$\begin{aligned}\mathcal{L} = {} & \tfrac{1}{2}M\dot{x}^2 + \tfrac{1}{2}m_1(\dot{x}^2 + l_1^2\cos^2\theta_1\dot{\theta}_1^2 - 2\dot{x}l_1\cos\theta_1\dot{\theta}_1) + \tfrac{1}{2}m_1l_1^2\sin^2\theta_1\dot{\theta}_1^2 + \\ & + \tfrac{1}{2}m_2(\dot{x}^2 + l_2^2\cos^2\theta_2\dot{\theta}_2^2 - 2\dot{x}l_2\cos\theta_2\dot{\theta}_2) + \tfrac{1}{2}m_2l_2^2\sin^2\theta_2\dot{\theta}_2^2 - \\ & - (M + m_1 + m_2)gl_1 - m_1gl_1\cos\theta_1 - m_2gl_2\cos\theta_2\end{aligned} \tag{7.8}$$

$$\begin{aligned}\mathcal{L} = {} & \tfrac{1}{2}(M + m_1 + m_2)\dot{x}^2 - (m_1l_1\cos\theta_1\dot{\theta}_1 + m_2l_2\cos\theta_2\dot{\theta}_2)\dot{x} + \\ & + \tfrac{1}{2}m_1l_1^2(\cos^2\theta_1 + \sin^2\theta_1)\dot{\theta}_1^2 + \tfrac{1}{2}m_2l_2^2(\cos^2\theta_2 + \sin^2\theta_2)\dot{\theta}_2^2 - \\ & - (M + m_1 + m_2)gl_1 - m_1gl_1\cos\theta_1 - m_2gl_2\cos\theta_2\end{aligned} \tag{7.9}$$

$$\begin{aligned}\mathcal{L} = {} & \tfrac{1}{2}(M + m_1 + m_2)\dot{x}^2 - (m_1l_1\cos\theta_1\dot{\theta}_1 + m_2l_2\cos\theta_2\dot{\theta}_2)\dot{x} + \tfrac{1}{2}m_1l_1^2\dot{\theta}_1^2 + \\ & + \tfrac{1}{2}m_2l_2^2\dot{\theta}_2^2 - (M + m_1 + m_2)gl_1 - m_1gl_1\cos\theta_1 - m_2gl_2\cos\theta_2 \quad ,\end{aligned} \tag{7.10}$$

and finally by using the Lagrange-d'Alembert Principle, [9]

$$\frac{d}{dt}\frac{\partial\mathcal{L}}{\partial\dot{\mathbf{q}}} - \frac{\partial\mathcal{L}}{\partial\mathbf{q}} = \mathbf{Q} \quad , \tag{7.11}$$

$$\mathbf{q} = \begin{bmatrix}\theta_1 \\ \theta_2 \\ x\end{bmatrix} \quad , \quad \mathbf{Q} = \begin{bmatrix}-b_{p_1,v}\dot{\theta}_1 - \tanh(\mathrm{k}_{\mathrm{tanh}}\dot{\theta}_1)b_{p_1,c} \\ -b_{p_2,v}\dot{\theta}_2 - \tanh(\mathrm{k}_{\mathrm{tanh}}\dot{\theta}_2)b_{p_2,c} \\ u - b_{c,v}\dot{x} - \tanh(\mathrm{k}_{\mathrm{tanh}}\dot{x})b_{c,c}\end{bmatrix} \quad . \tag{7.12}$$

Note that, as in *Part 1*, the control output is seen as the force on the cart directly, $u = F$, to avoid excessive notation. Equation 7.11 is computed for each generalized coordinate starting with the first pendulum angle, θ_1,

$$\frac{d}{dt}\frac{\partial\mathcal{L}}{\partial\dot{\theta}_1} - \frac{\partial\mathcal{L}}{\partial\theta_1} = Q_1 \tag{7.13}$$

$$m_1l_1\sin\theta_1\dot{\theta}_1\dot{x} - m_1l_1\cos\theta_1\ddot{x} + m_1l_1^2\ddot{\theta}_1 - m_1l_1\sin\theta_1\dot{\theta}_1\dot{x} - m_1gl_1\sin\theta_1 = Q_1 \tag{7.14}$$

$$-m_1l_1\cos\theta_1\ddot{x} + m_1l_1^2\ddot{\theta}_1 - m_1gl_1\sin\theta_1 = -b_{p_1,v}\dot{\theta}_1 - \tanh(\mathrm{k}_{\mathrm{tanh}}\dot{\theta}_1)b_{p_1,c} \quad , \tag{7.15}$$

similarly for the second pendulum angle, θ_2,

$$-m_2l_2\cos\theta_2\ddot{x} + m_2l_2^2\ddot{\theta}_2 - m_2gl_2\sin\theta_2 = -b_{p_2,v}\dot{\theta}_2 - \tanh(\mathrm{k}_{\mathrm{tanh}}\dot{\theta}_2)b_{p_2,c} \quad , \tag{7.16}$$

and finally for the cart position, x,

$$\frac{d}{dt}\frac{\partial\mathcal{L}}{\partial\dot{x}} - \frac{\partial\mathcal{L}}{\partial x} = Q_3 \tag{7.17}$$

$$\begin{aligned}&(M + m_1 + m_2)\ddot{x} + m_1l_1\sin\theta_1\dot{\theta}_1^2 - m_1l_1\cos\theta_1\ddot{\theta}_1 + \\ &+ m_2l_2\sin\theta_2\dot{\theta}_2^2 - m_2l_2\cos\theta_2\ddot{\theta}_2 = u - b_{c,v}\dot{x} - \tanh(\mathrm{k}_{\mathrm{tanh}}\dot{x})b_{c,c} \quad .\end{aligned} \tag{7.18}$$

The final dynamic equations for the twin pendulum system are then,

$$-m_1 l_1 \cos\theta_1 \ddot{x} + m_1 l_1^2 \ddot{\theta}_1 - m_1 g l_1 \sin\theta_1 = Q_1 \tag{7.19}$$

$$-m_2 l_2 \cos\theta_2 \ddot{x} + m_2 l_2^2 \ddot{\theta}_2 - m_2 g l_2 \sin\theta_2 = Q_2 \tag{7.20}$$

$$(M + m_1 + m_2)\ddot{x} + m_1 l_1 \sin\theta_1 \dot{\theta}_1^2 - m_1 l_1 \cos\theta_1 \ddot{\theta}_1 + m_2 l_2 \sin\theta_2 \dot{\theta}_2^2 - m_2 l_2 \cos\theta_2 \ddot{\theta}_2 = Q_3 \quad . \tag{7.21}$$

If one of the angles are fixed in these equations, that is, θ_1 or θ_2 and its derivatives are set to zero, then the system reduces to the cart pendulum system from *Part 1* with added mass from the extra pendulum. This added mass appears in the equations as an increase in cart mass, which makes sense as the pendulum is fixed to the cart in this scenario.
As for the cart pendulum system from *Part 1*, by arranging the dynamic equations,

$$\begin{bmatrix} m_1 l_1^2 & 0 & -m_1 l_1 \cos\theta_1 \\ 0 & m_2 l_2^2 & -m_2 l_2 \cos\theta_2 \\ -m_1 l_1 \cos\theta_1 & -m_2 l_2 \cos\theta_2 & M + m_1 + m_2 \end{bmatrix} \begin{bmatrix} \ddot{\theta}_1 \\ \ddot{\theta}_2 \\ \ddot{x} \end{bmatrix} + \begin{bmatrix} 0 \\ 0 \\ m_1 l_1 \sin\theta_1 \dot{\theta}_1^2 + m_2 l_2 \sin\theta_2 \dot{\theta}_2^2 \end{bmatrix} + \\ + \begin{bmatrix} -b_{p_1,v}\dot{\theta}_1 - \tanh(\mathrm{k}_{\mathrm{tanh}}\dot{\theta}_1) b_{p_1,c} \\ -b_{p_2,v}\dot{\theta}_2 - \tanh(\mathrm{k}_{\mathrm{tanh}}\dot{\theta}_2) b_{p_2,c} \\ -b_{c,v}\dot{x} - \tanh(\mathrm{k}_{\mathrm{tanh}}\dot{x}) b_{c,c} \end{bmatrix} + \begin{bmatrix} -m_1 g l_1 \sin\theta_1 \\ -m_2 g l_2 \sin\theta_2 \\ 0 \end{bmatrix} = \begin{bmatrix} 0 \\ 0 \\ u \end{bmatrix} \quad , \tag{7.22}$$

the well known general form of an m-link robot is obtained, [12, 13]

$$\mathbf{M}(\mathbf{q})\ddot{\mathbf{q}} + \mathbf{C}(\mathbf{q}, \dot{\mathbf{q}}) + \mathbf{B}(\dot{\mathbf{q}}) + \mathbf{G}(\mathbf{q}) = \mathbf{F} \quad , \tag{7.23}$$

where,

$\mathbf{M}(\mathbf{q})$	is the inertia matrix
$\mathbf{C}(\mathbf{q}, \dot{\mathbf{q}})$	is the Coriolis and centrifugal effects
$\mathbf{B}(\dot{\mathbf{q}})$	is the friction
$\mathbf{G}(\mathbf{q})$	is the force due to gravity
$\mathbf{F}$	is the input force vector .

Choosing states $[\, x_1 \;\; x_2 \;\; x_3 \; x_4 \;\; x_5 \;\; x_6 \,]^{\mathrm{T}} = [\, \theta_1 \;\; \theta_2 \;\; x \;\; \dot{\theta}_1 \;\; \dot{\theta}_2 \;\; \dot{x} \,]^{\mathrm{T}}$ results in the nonlinear state space representation,

$$\begin{bmatrix} \dot{x_1} \\ \dot{x_2} \\ \dot{x_3} \\ \dot{x_4} \\ \dot{x_5} \\ \dot{x_6} \end{bmatrix} = \begin{bmatrix} x_4 \\ x_5 \\ x_6 \\ \\ \mathbf{M}^{-1}(x_1, x_2)(\mathbf{F} - \mathbf{C}(x_1, x_2, x_4, x_5) - \mathbf{B}(x_4, x_5, x_6) - \mathbf{G}(x_1, x_2)) \\ \\ \end{bmatrix} . \tag{7.24}$$

8 | Swing-Up Design

This chapter contains a swing-up design for the twin pendulum system. As for the cart pendulum system in *Part 1* the design is based on [14]. The presented approach is similar to the sat-based energy controller, the final design from *Part 1.* Detailed nonlinear analysis is left out here since this design exploits the same principals as for the final cart pendulum swing-up controller in *Part 1.*
Both pendulums are started in π at rest and the design is based on the pendulum energies in the coordinate system fixed to the cart, thus reducing the generalized coordinates to,

$$\begin{cases} x_{p_1} = -l_1 \sin\theta_1 \\ y_{p_1} = l_1 + l_1 \cos\theta_1 \end{cases} \begin{cases} x_{p_2} = -l_2 \sin\theta_2 \\ y_{p_2} = l_1 + l_2 \cos\theta_2 \end{cases} \begin{cases} \dot{x}_{p_1} = -l_1 \cos\theta_1 \dot{\theta}_1 \\ \dot{y}_{p_1} = -l_1 \sin\theta_1 \dot{\theta}_1 \end{cases} \begin{cases} \dot{x}_{p_2} = -l_2 \cos\theta_2 \dot{\theta}_2 \\ \dot{y}_{p_2} = -l_2 \sin\theta_2 \dot{\theta}_2 \end{cases} . \tag{8.1}$$

Since the energies of the two pendulums are described in a local coordinate system fixed to the cart, there is no cross-coupling, thus the energies are independent of one another,

$$E_{p_1} = m_1 g y_{p_1} + \tfrac{1}{2} m_1 \dot{x}_{p_1}^2 + \tfrac{1}{2} m_1 \dot{y}_{p_1}^2 \tag{8.2}$$
$$E_{p_2} = m_2 g y_{p_2} + \tfrac{1}{2} m_2 \dot{x}_{p_2}^2 + \tfrac{1}{2} m_2 \dot{y}_{p_2}^2 \quad , \tag{8.3}$$

and in generalized coordinates,

$$E_{p_1} = \tfrac{1}{2} J_1 \dot{\theta}_1^2 + m_1 g l_1 (\cos\theta_1 + 1) \tag{8.4}$$
$$E_{p_2} = \tfrac{1}{2} J_2 \dot{\theta}_2^2 + m_2 g (l_2 \cos\theta_2 + l_1) \quad , \tag{8.5}$$

where the inertia $J_1 = m_1 l_1^2$ and $J_2 = m_2 l_2^2$ and the energy in equilibrium for each pendulum is,

$$E_{eq_1} = 2 m_1 g l_1 \quad , \quad E_{eq_2} = m_2 g (l1 + l2) \quad , \tag{8.6}$$

such that,

$$E_{\Delta_1} = E_{p_1} - E_{eq_1} = \tfrac{1}{2} J_1 \dot{\theta}_1^2 + m_1 g l_1 (\cos\theta_1 - 1) \tag{8.7}$$
$$E_{\Delta_2} = E_{p_2} - E_{eq_2} = \tfrac{1}{2} J_2 \dot{\theta}_2^2 + m_2 g l_2 (\cos\theta_2 - 1) \quad . \tag{8.8}$$

Choosing the function candidate,

$$V(\theta_1, \theta_2, \dot{\theta}_1, \dot{\theta}_2) = \tfrac{1}{2} E_{\Delta_1}^2 + \tfrac{1}{2} E_{\Delta_1}^2 \quad , \tag{8.9}$$

and with the dynamics given by,

$$J\ddot{\theta} = m_1 l_1 \cos\theta_1 a_c + m_1 g l_1 \sin\theta_1 \tag{8.10}$$
$$J\ddot{\theta} = m_2 l_2 \cos\theta_2 a_c + m_2 g l_2 \sin\theta_2 \quad , \tag{8.11}$$

the derivative of V is evaluated along trajectories of the system,

$$\dot{V} = E_{\Delta_1}\dot{E}_{\Delta_1} + E_{\Delta_2}\dot{E}_{\Delta_2} \tag{8.12}$$

$$\begin{aligned}\dot{V} = {} & E_{\Delta_1}(J_1\dot{\theta}_1\ddot{\theta}_1 - m_1 g l_1 \sin\theta_1\dot{\theta}_1) \\ & + E_{\Delta_2}(J_2\dot{\theta}_2\ddot{\theta}_2 - m_2 g l_2 \sin\theta_2\dot{\theta}_2)\end{aligned} \tag{8.13}$$

$$\begin{aligned}\dot{V} = {} & E_{\Delta_1}(\dot{\theta}_1(m_1 l_1 \cos\theta_1 a_c + m_1 g l_1 \sin\theta_1) - m_1 g l_1 \sin\theta_1\dot{\theta}_1) \\ & + E_{\Delta_2}(\dot{\theta}_2(m_2 l_2 \cos\theta_2 a_c + m_2 g l_2 \sin\theta_2) - m_2 g l_2 \sin\theta_2\dot{\theta}_2)\end{aligned} \tag{8.14}$$

$$\dot{V} = G a_c \quad , \tag{8.15}$$

where,

$$G = m_1 l_1 E_{\Delta_1} \cos\theta_1\dot{\theta}_1 + m_2 l_2 E_{\Delta_2} \cos\theta_2\dot{\theta}_2 \quad . \tag{8.16}$$

Following control law for the pivot point acceleration, a_c, is chosen such that $\dot{V}$ is negative semi-definite,

$$a_c = sat(-kG) \quad , \tag{8.17}$$

where k is a tuning parameter and,

$$\text{sat}(s) = \begin{cases} s & |s| \le a_{max} \\ \text{sgn}(s)\ a_{max} & |s| > a_{max} \end{cases} \quad . \tag{8.18}$$

This control law exhibits the same properties as the first design in *Part 1*, thus the largest invariant set also contains the stable equilibrium at π, which is the starting position of the pendulums. For this design, the issue is solved by applying a large current, $i_{max} = 4.58\,\text{A}$, for $0.1\,\text{s}$ before initiating the swing-up sequence, thus starting at some initial values for which the control signal is different from zero.
The controller for cart position from *Part 1* is used unchanged in this design.

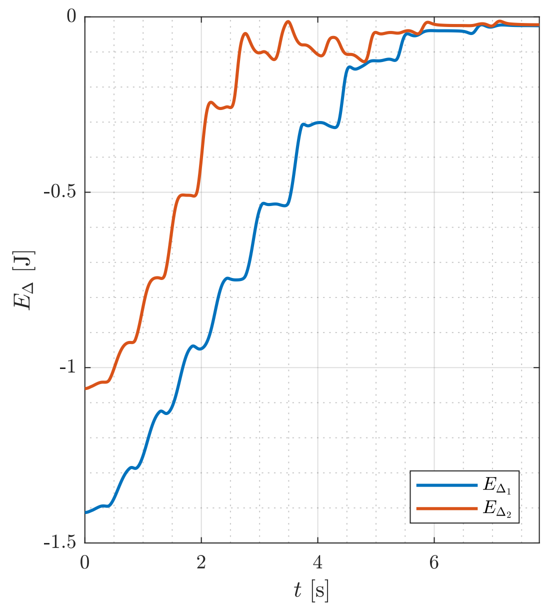

Figure 8.1: The mechanical energy for each pendulum approach that of their respective equilibrium points shown here by difference in energy.

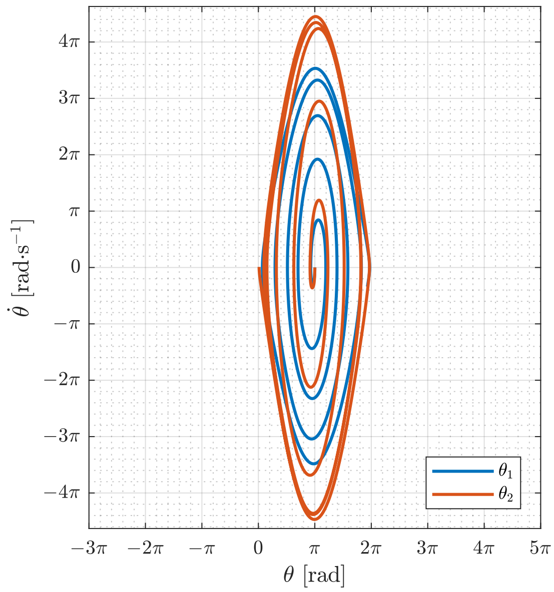

Figure 8.2: Both pendulums of the twin system successfully reaches their heteroclinic orbit. Notice how the shorter pendulum (red) reaches higher angular velocity at its orbit than the longer pendulum (blue), which makes sense as the shorter pendulum has a higher frequency.

The design is implemented for simulation, see Figure 8.1 and 8.2, effectively driving the energy differences to zero and reaching a heteroclinic orbit for both pendulums. In these simulations the gain is chosen to $k = 16$ and 0.022 J is added to the energy references to reach orbit. In Figure 8.3 and 8.4 it is seen that though the two pendulums reach their heteroclinic orbits, they do not necessarily reach equilibrium simultaneously. However, using a wrapped version of the angles, same as in *Part 1*, it is possible to catch both pendulums while in opposing equilibrium points. Such a scenario is seen most clearly at the end in Figure 8.3 and 8.4 about 11 swings into the simulation.

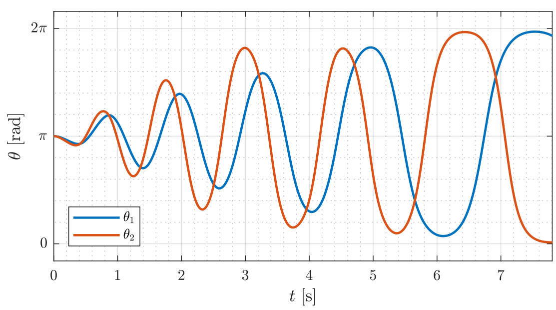

Figure 8.3: Due to different lengths of the two pendulums the frequencies are different thus the signals drift compared to one another.

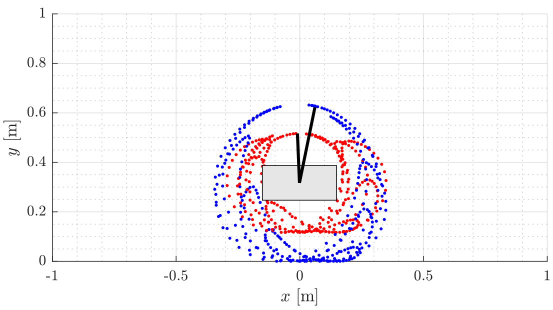

Figure 8.4: The two pendulums meet in upright position but at opposing equilibrium points.

The control signal used to obtain the behavior in these simulations are shown in Figure 8.5.

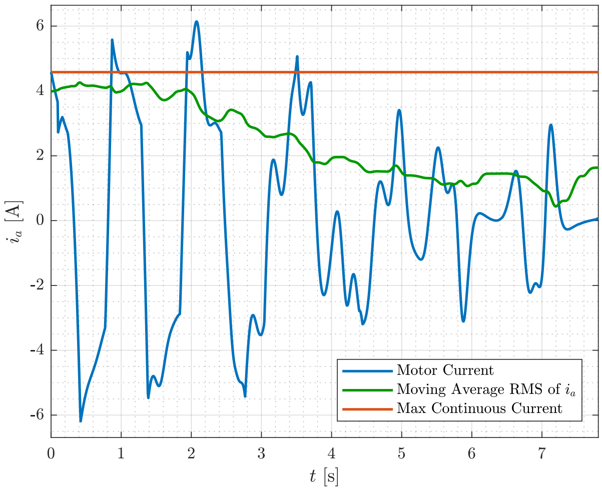

Figure 8.5: The control signal required for the twin pendulum swing-up behavior simulated in this chapter is within the limits of the motor.

Figure 8.6 and 8.7 shows that the position control from *Part 1* also works well with the twin pendulum swing-up design.

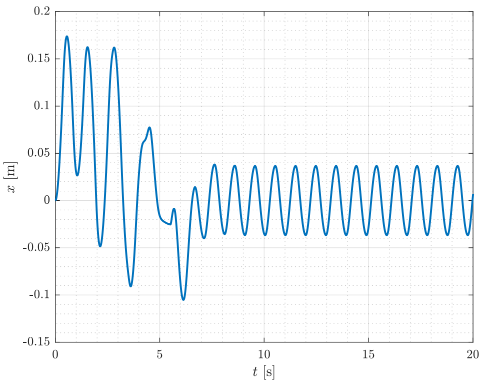

Figure 8.6: The position control design used in *Part 1* also shows good results for the twin pendulum.

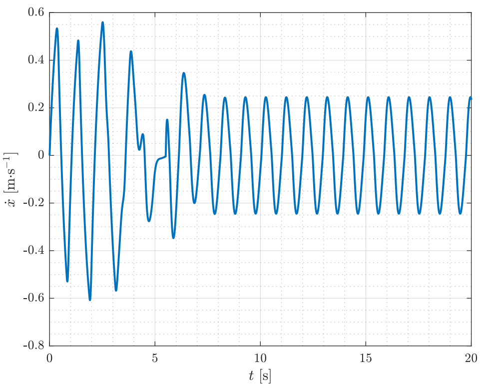

Figure 8.7: Both states, x and $\dot{x}$, are successfully brought to around zero while still allowing the swing-up controller to maintain orbit.

9 | Stabilization

In this chapter a Linear Quadratic Regulator (LQR) is designed to stabilize the twin pendulum in upright position taking over from the swing-up controller.
The nonlinear state space system from Equation 7.24 are linearized,

$$\mathbf{A} = \frac{\partial \mathbf{f}(\mathbf{x})}{\partial \mathbf{x}}\bigg|_{\substack{\mathbf{x}=\mathbf{0}\\ u=0\\ \mathrm{k_{tanh}}=1}} \quad , \quad \mathbf{B} = \frac{\partial \mathbf{f}(\mathbf{x})}{\partial u}\bigg|_{\substack{\mathbf{x}=\mathbf{0}\\ u=0\\ \mathrm{k_{tanh}}=1}} \quad , \tag{9.1}$$

$$\mathbf{A} = \begin{bmatrix} 0 & 0 & 0 & 1 & 0 & 0 \\ 0 & 0 & 0 & 0 & 1 & 0 \\ 0 & 0 & 0 & 0 & 0 & 1 \\ \frac{g(M+m_1)}{Ml_1} & \frac{gm_2}{Ml_1} & 0 & -\frac{(M+m_1)(b_{p_1,c}+b_{p_1,v})}{Ml_1^2 m1} & -\frac{b_{p_2,c}+b_{p_2,v}}{Ml_1 l_2} & 0 \\ \frac{gm_1}{Ml_2} & \frac{g(M+m_2)}{Ml_2} & 0 & -\frac{b_{p_1,c}+b_{p_1,v}}{Ml_1 l_2} & -\frac{(M+m2)(b_{p_2,c}+b_{p_2,v})}{Ml_2^2 m_2} & 0 \\ \frac{gm_1}{M} & \frac{gm_2}{M} & 0 & -\frac{b_{p_1,c}+b_{p_1,v}}{Ml_1} & -\frac{b_{p_2,c}+b_{p_2,v}}{Ml_2} & 0 \end{bmatrix} \tag{9.2}$$

$$\mathbf{B} = \begin{bmatrix} 0 & 0 & 0 & \frac{1}{Ml_1} & \frac{1}{Ml_2} & \frac{1}{M} \end{bmatrix}^{\mathrm{T}} \quad . \tag{9.3}$$

The controllability and observability matrices are computed for the linearized system,

$$\boldsymbol{\mathcal{C}} = \begin{bmatrix} \mathbf{B} & \mathbf{AB} & \mathbf{A}^2\mathbf{B} & \mathbf{A}^3\mathbf{B} & \mathbf{A}^4\mathbf{B} & \mathbf{A}^5\mathbf{B} \end{bmatrix} \Rightarrow \mathrm{rank}(\boldsymbol{\mathcal{C}}) = 6 \tag{9.4}$$

$$\boldsymbol{\mathcal{O}} = \begin{bmatrix} \mathbf{C} \\ \mathbf{CA} \\ \mathbf{CA}^2 \\ \mathbf{CA}^3 \\ \mathbf{CA}^4 \\ \mathbf{CA}^5 \end{bmatrix} \Rightarrow \mathrm{rank}(\boldsymbol{\mathcal{O}}) = 6 \quad , \tag{9.5}$$

and since $\boldsymbol{\mathcal{C}}$ and $\boldsymbol{\mathcal{O}}$ both have full rank, the system is controllable and observable. It is interesting to note that if friction is set to zero and both pendulums are given same length, then $\boldsymbol{\mathcal{C}}$ looses rank, that is, the system would no longer be controllable. This is true even if the pendulum masses are different.

minimizing the cost function

$$\mathcal{J} = \int_0^\infty \mathbf{x}^T\mathbf{Q}\mathbf{x} + \mathbf{u}^T\mathbf{R}\mathbf{u}\; dt \quad . \tag{9.6}$$

Bryson's rule

$$Q_{ii} = \frac{1}{x_{i,max}} \quad , \quad R_{ii} = \frac{1}{u_{i,max}} \tag{9.7}$$

where $x_{i,max}$ are the maximum state errors and $u_{i,max}$ are the maximum inputs.

state-transfer matrix P

$$\mathbf{F} = -\mathbf{R}^{-1}\mathbf{B}^T\mathbf{P} \tag{9.8}$$

Algebraic Riccatti equation

$$\mathbf{A}^T\mathbf{P} + \mathbf{P}\mathbf{A} - \mathbf{P}\mathbf{B}\mathbf{R}^{-1}\mathbf{B}^T\mathbf{P} + \mathbf{Q} = \mathbf{0} \tag{9.9}$$

In this case there is only one input u so R is scalar. The tuned $\mathbf{Q}$ and R are given by,

$$\mathbf{Q} = diag(1,\ 1,\ \tfrac{1}{0.028},\ 1,\ 1,\ 1) \quad , \quad R = \frac{1}{3.3357} \quad , \tag{9.10}$$

gain vector

$$\mathbf{K} = \begin{bmatrix} -2742.93 & 2302.58 & 107.09 & -493.15 & 328.26 & 105.18 \end{bmatrix} \tag{9.11}$$

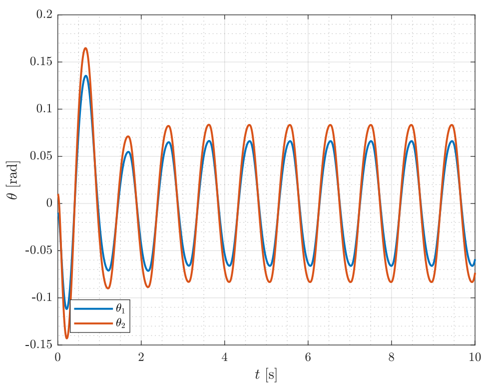

Figure 9.1: a

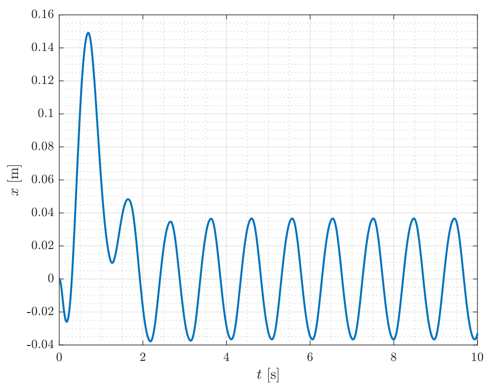

Figure 9.2: a

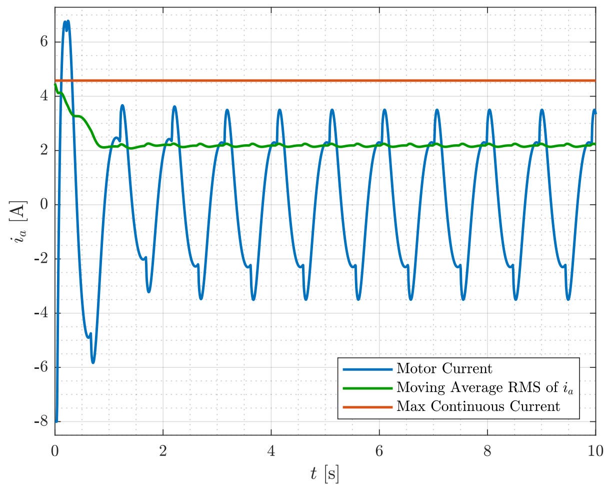

Figure 9.3: a

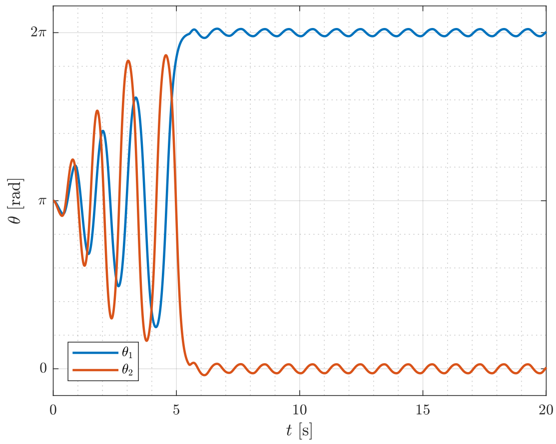

Figure 9.4: a

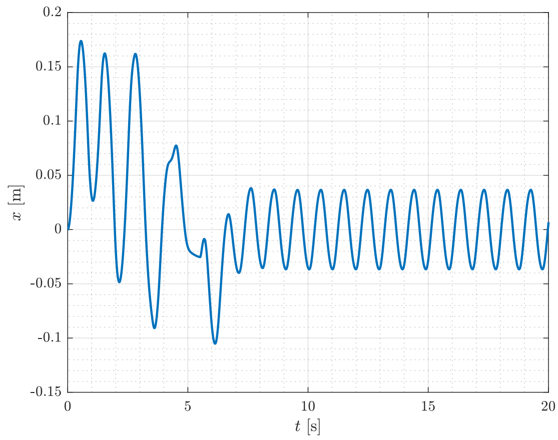

Figure 9.5: a

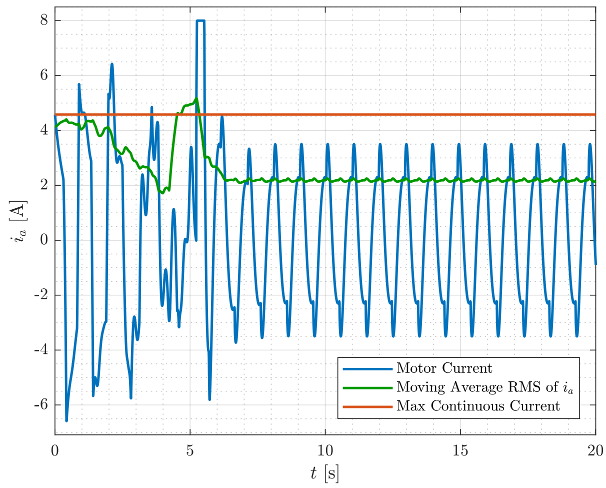

Figure 9.6: a

10 | State Estimation

Kalman filter top

quantization model

$$x_q = \Delta \left\lfloor \frac{x}{\Delta} + \frac{1}{2} \right\rfloor \quad , \tag{10.1}$$

for x $\Delta_x = 0.088 \times 10^{-3}\,\mathrm{m/tic}$
with $\Delta_\theta = \pi \times 10^{-3}\,\mathrm{rad/tic}$ and applying the quantization model to a smoothed version of the original measured signal is seen in Figure 10.1.

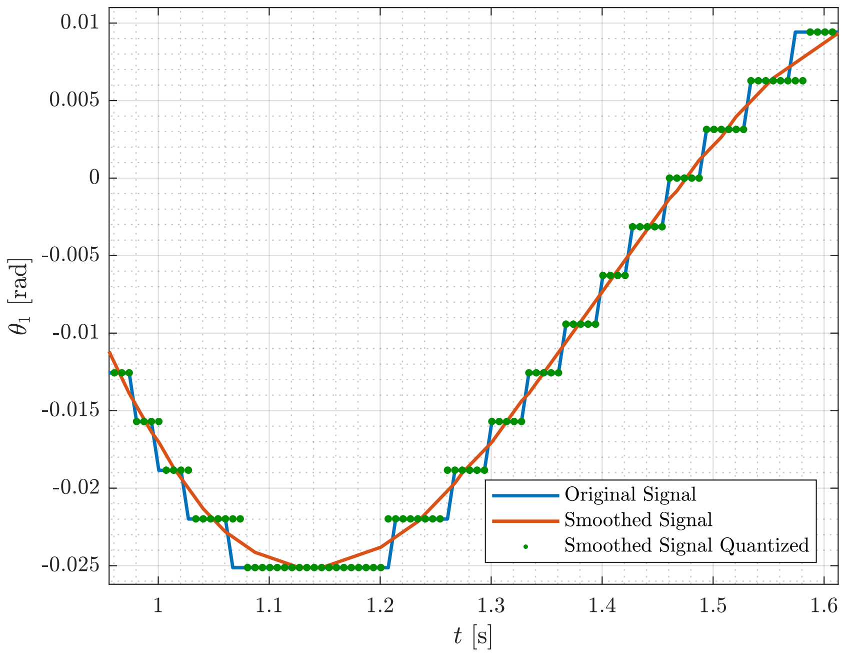

Figure 10.1: a

Model

$$\mathbf{x}_k = \mathbf{F}\mathbf{x}_{k-1} + \mathbf{G}u_{k-1} + \mathbf{w}_{k-1} \quad , \qquad \mathbf{w} \sim \mathcal{N}(0,\, \mathbf{Q}) \tag{10.2}$$

$$\mathbf{y}_k = \mathbf{H}\mathbf{x}_k + \mathbf{v}_k \quad , \qquad \mathbf{v} \sim \mathcal{N}(0,\, \mathbf{R}) \quad , \tag{10.3}$$

Initialization

The previous predicted state vector, $\hat{\mathbf{x}}_{k-1}$ is initialized to the current measurements y_k,

$$\hat{\mathbf{x}}_{k-1} = y_k \quad , \tag{10.4}$$

and the previous state error covariance $\mathbf{P}_{k-1}$ is initialized to some initial guess $\mathbf{P}_0$ here set to the identity matrix,

$$\mathbf{P}_{k-1} = \mathbf{P}_0 \quad . \tag{10.5}$$

When the Kalman filter is running $\mathbf{P}$ will converge to some steady state values which is then be used as $\mathbf{P}_0$ in the implementation for faster convergence.

Prediction

$$\hat{\mathbf{x}}_{k|k-1} = \mathbf{F}\hat{\mathbf{x}}_{k-1} + \mathbf{G}u_{k-1} \quad . \tag{10.6}$$

$$\mathbf{P}_{k|k-1} = \mathbf{F}P_{k-1}\mathbf{F}^{\mathrm{T}} + \mathbf{Q} \quad . \tag{10.7}$$

$k|k-1$ reads "k given $k-1$".

Update

$$\mathbf{K}_k = \mathbf{P}_{k|k-1}\mathbf{H}^{\mathrm{T}}(\mathbf{H}\mathbf{P}_{k|k-1}\mathbf{H}^{\mathrm{T}} + \mathbf{R})^{-1} \quad . \tag{10.8}$$

$$\hat{\mathbf{x}}_k = \hat{\mathbf{x}}_{k-1} + \mathbf{K}_k(y_k - \mathbf{H}\hat{\mathbf{x}}_{k-1}) \quad . \tag{10.9}$$

where $\mathbf{H}\hat{\mathbf{x}}_{k-1} = \hat{\mathbf{y}}_{k-1}$ is the predicted output.

$$\mathbf{P}_k = (\mathbf{I} - \mathbf{K}_k\mathbf{H})\mathbf{P}_{k|k-1} \quad . \tag{10.10}$$

The measurement noise covariance is tuned such that the quantization problem is solved, see Figure 10.2,

$$\mathbf{R} = diag(100,\ 100,\ 10) \quad . \tag{10.11}$$

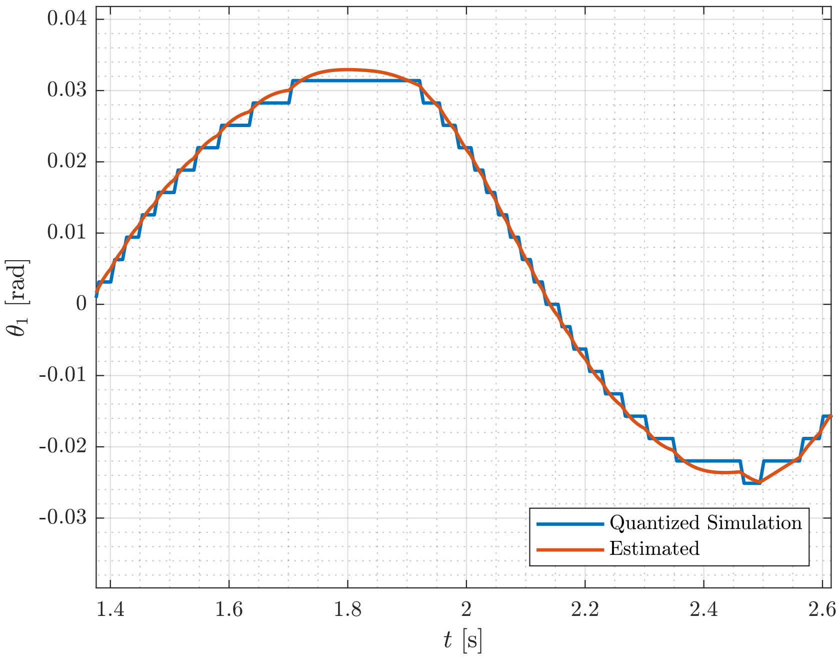

Figure 10.2: a

The process noise covariance matrix is tuned to get as true estimations of the drivatives as possible while maintaining low noise levels,

$$\mathbf{Q} = diag(1,\ 1,\ 1,\ 100,\ 100,\ 10) \quad , \tag{10.12}$$

see simulation in Figure 10.3.

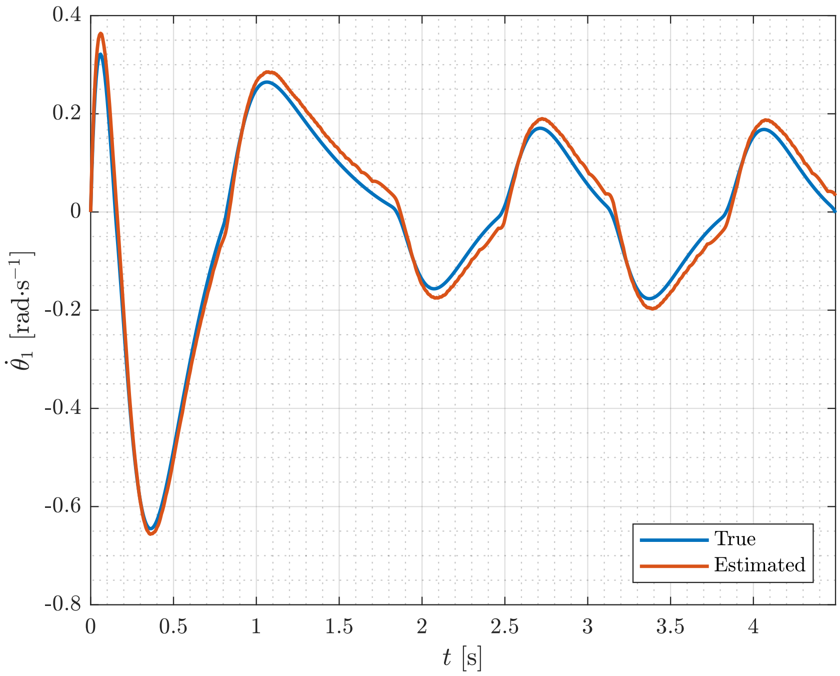

Figure 10.3: a

Very similar results are obtained for the second pendulum. Since the quantization problem is more than an order of magnitude smaller for the position measurements compared to the angle measurements, the filter obtains near perfect results in simulation, see Figure 10.4 and 10.5.

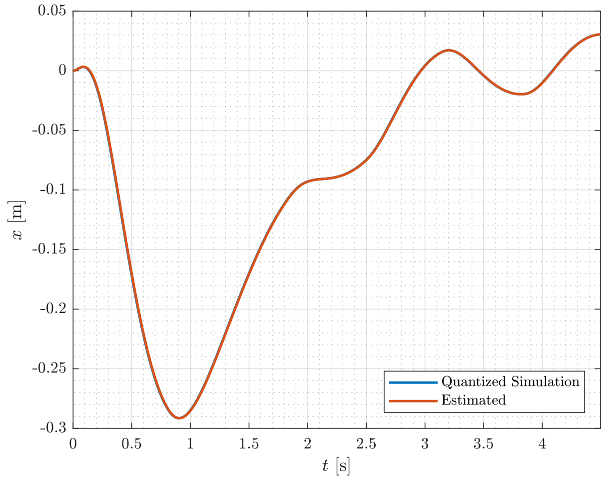

Figure 10.4: a

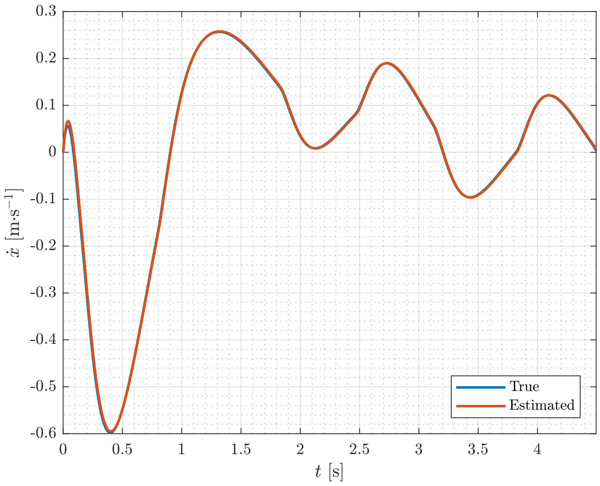

Figure 10.5: a

11 | Results

12 | Conclusion

Bibliography

[1] *Maxon RE Motor*. Oct. 8, 2018. URL: https://www.maxonmotor.com/medias/sys_master/root/8825409470494/17-EN-133.pdf.

[2] Avago Technologies. *HEDM-55xx/560x & HEDS-55xx/56xx*. Aug. 15, 2018. URL: https://www.infineon.com/dgdl/Infineon-Encoder_HEDS-5540-A14-AP-v01_00-EN.pdf?fileId=5546d46147a9c2e40147d3d593970357.

[3] *Maxon Controller*. Aug. 15, 2018. URL: https://www.maxonmotor.com/maxon/view/product/control/Servoverstaerker-4-Q-DC/201583.

[4] *sparkfun Teensy 3.6*. Aug. 15, 2018. URL: https://www.sparkfun.com/products/14057.

[5] *HCTL-2021 PLC Avago Datasheet*. Aug. 15, 2018. URL: https://datasheet.octopart.com/HCTL-2021-PLC-Avago-datasheet-7580518.pdf.

[6] *K66 Sub-Family Reference Manual*. Aug. 15, 2018. URL: https://cdn.sparkfun.com/datasheets/Dev/Arduino/Boards/K66P144M180SF5RMV2.pdf.

[7] Jonas Ørndrup Jesper H. Hørgensen. *Non-linear Control and Machine Learning on an Inverted Pendulum on a Cart. Master Thesis*. 2018.

[8] Niels Skov Vestergaard. *Sliding Mode Stabilization and Phase Plane Trajectory Planning for a Cart Pendulum System. 9th Semester Project*. 2018.

[9] Rafael Wisniewski. *Mechanical Systems II. Lagrange Mechanics*. Aalborg University, 2013.

[10] Charles M. Close, Dean K. Frederick, and Jonathan C. Newell. *Modeling and Analysis of Dynamic Systems*. Wiley, 2001.

[11] H. Olsson et al. *Friction Models and Friction Compensation*. Nov. 28, 1997.

[12] Mark W. Spong, Seth Hutchinson, and M. Vidyasagar. *Robot Dynamics and Control*. 2nd ed. Wiley, 2005.

[13] Lorenzo Sciavicco and Bruno Siciliano. *Modelling and Control of Robot Manipulators*. 2nd ed. Lorenzo Sciavicco and Bruno Siciliano. London: Springer, 2012.

[14] Karl Johan Åström and Katsuhisa Furuta. "Swinging up a pendulum by energy control". In: *Automatica* 36.2 (2000), pp. 287–295.

[15] Hassan K. Khalil. *Nonlinear Systems*. 3rd ed. 2015.

[16] Morten H. Knudsen. "Experimental modeling of dynamic systems: an educational approach". In: *IEEE Transactions on Education* 49.1 (Feb. 2006), pp. 29–38.

Swing-up and Stabilization of a Cart Pendulum and Twin Pendulum System

Using Nonlinear Control Strategies

Niels Skov Vestergaard

January 2019

Control & Automation

Aalborg University
Department of Electronic Systems
Fredrik Bajers Vej 7
9220 Aalborg Øst

AALBORG UNIVERSITY
DENMARK